JOURNAL OF THE AMERICAN CHEMICAL SOCIETY

pubs.acs.org/JACS Article

Microtubule-Targeting NAP Peptide-Ru(II)-polypyridyl Conjugate As a Bimodal Therapeutic Agent for Triple Negative Breast Carcinoma

Atin Chatterjee, Sandip Sarkar, Sangheeta Bhattacharjee,[▽] Arpan Bhattacharyya,[▽] Surajit Barman, Uttam Pal, Raviranjan Pandey, Anitha Ethirajan,* Batakrishna Jana,* Benu Brata Das,* and Amitava Das*

Cite This: *J. Am. Chem. Soc.* 2025, 147, 532−547

Read Online

ACCESS | Metrics & More | Article Recommendations | Supporting Information

ABSTRACT: Triple-negative breast cancer (TNBC) poses significant treatment challenges due to its high metastasis, heterogeneity, and poor biomarker expression. The N-terminus of an octapeptide NAPVSIPQ (**NAP**) was covalently coupled to a carboxylic acid derivative of Ru(2,2′-bipy)$_3^{2+}$ (**Rubpy**) to synthesize an N-stapled short peptide-Rubpy conjugate (**Ru-NAP**). This photosensitizer (PS) was utilized to treat TNBC through microtubule (MT) targeted chemotherapy and photodynamic therapy (PDT). **Ru-NAP** formed more elaborate molecular aggregates with fibrillar morphology as compared to **NAP**. A much higher binding affinity of **Ru-NAP** over **NAP** toward β-tubulin ($K_{\text{Ru-NAP}}$: $(6.8 \pm 0.55) \times 10^6$ M^{-1}; K_{NAP}: $(8.2 \pm 1.1) \times 10^4$ M^{-1}) was observed due to stronger electrostatic interactions between the MT with an average linear charge density of ∼85 e/nm and the cationic **Rubpy** part of **Ru-NAP**. This was also supported by docking, simulation, and appropriate imaging studies. **Ru-NAP** promoted serum stability, specific binding of **NAP** to the E-site of the β^{III}-tubulin followed by the disruption of the MT network, and effective singlet oxygen generation in TNBC cells (MDA-MB-231), causing cell cycle arrest in the G2/M phase and triggering apoptosis. Remarkably, MDA-MB-231 cells were more sensitive to **Ru-NAP** compared to noncancerous human embryonic kidney (HEK293 cells) when exposed to light (${}^{\text{Light}}\text{IC}_{50}{}^{\text{Ru-NAP}}$[HEK293]: 17.2 ± 2.5 μM, compared to ${}^{\text{Light}}\text{IC}_{50}{}^{\text{Ru-NAP}}$[MDA-MB-231]: 32.5 ± 7.8 nM, ${}^{\text{Dark}}\text{IC}_{50}{}^{\text{Ru-NAP}}$[HEK293]: > 80 μM, compared to ${}^{\text{Dark}}\text{IC}_{50}{}^{\text{Ru-NAP}}$[MDA-MB-231]: 2.9 ± 0.5 μM). **Ru-NAP** also effectively inhibited tumor growth in MDA-MB-231 xenograft models in nude mice. Our findings provide strong evidence that **Ru-NAP** has a potential therapeutic role in TNBC treatment.

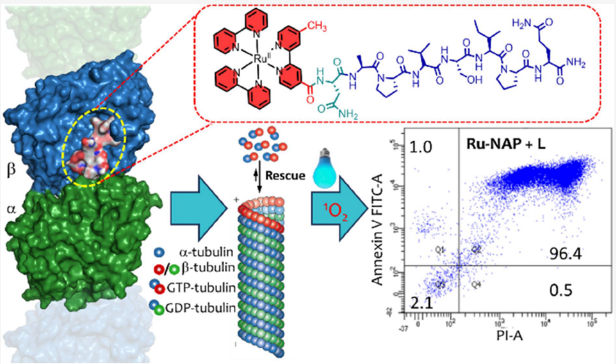

■ INTRODUCTION

Triple-negative breast cancer (TNBC) is a highly metastatic, heterogeneous breast cancer with impaired expression of estrogen (ER), progesterone (PR), and human epidermal growth factor receptor 2 (HER2).[1,2] Poor prognosis and its low response to therapeutics add to therapeutic challenges compared to non-TNBC cases.[3] Recent reports confirm that microtubule (MT) cytoskeletons are validated targets for breast cancer therapy.[4,5] MTs are associated with critical cellular functions including mitosis, cell signaling, intracellular trafficking, and angiogenesis.[6] Any molecule that can modulate the MT dynamics would induce the spindle checkpoint, arresting cell-cycle progression at mitosis and subsequent cell death. MT stabilizers stimulate the assembly of purified tubulin and shift the equilibrium of tubulin polymer from the soluble to the polymerized form.[7−9] This leads to consequential disruption of MT dynamics and mitotic arrest of cancer cells, which has been effectively utilized as a treatment strategy for cancer.[6,10−12] MTs are present both in interphase cells and in dividing cells in mammalian cells. These constitute the highly dynamic mitotic spindle and this accounts for the extreme sensitivity toward therapeutic inhibitors.[6] MT targeting agents (MTAs) are a type of vascular disrupting agents (VDAs).[5] Chemotherapeutic drugs that bind to the colchicine site of tubulin target tumor vasculature to induce blood vessel disruption are used in clinical trials.[13,14] Certain vinca alkaloids and taxanes are part of the FDA-approved drugs for treating hematological malignancies and solid tumors.[15,16] Taxol belongs to the taxane family and is being used for treating early-stage, advanced, and metastatic breast cancer.[17] A 3.5-Å resolution electron crystallography structure of the tubulin

Received: August 27, 2024
Revised: December 12, 2024
Accepted: December 12, 2024
Published: December 26, 2024

dimer bound to taxol reveals that taxol binds stoichiometrically and specifically to the β-tubulin subunit in MTs.[15] A few of the most recent and effective cancer chemotherapeutic drugs are derived from natural compounds that target MTs and disrupt the normal function of the mitotic spindle.[18] Site-specific binding of such molecules, either to soluble tubulin or to the MT governs the efficacy of these drugs as chemotherapeutic agents.[11] The major issues that limit the clinical efficacy of taxanes as the MTAs are low solubility and thus bioavailability, a relatively short circulation time $t_{1/2}$ (~1 h), inability to cross the blood-brain barrier, high systemic toxicity (e.g., neutropenia, neurotoxicity, genotoxicity, cardiac toxicity, repression of bone marrow, etc.) and the onset of multidrug resistance mechanisms.[17,19] These challenges offer a distinct scope for adopting an alternate strategy in developing MTAs for improved clinical efficacy toward cancer therapy.

NAPVSIPQ (Asn-Ala-Pro-Val-Ser-Ile-Pro-Gln; all amino acids are in L- form) abbreviated as **NAP** is a neuroprotective octapeptide derived from activity-dependent neuroprotective protein (ADNP). Affinity chromatography identified the β^{III}-tubulin as a major **NAP**-binding protein.[20] Presumably, binding of **NAP** to β^{III}-tubulin induces a conformational shift to facilitate tubulin polymerization with the E-site of the β^{III}-tubulin, which is preferentially occupied by guanosine triphosphate (GTP) rather than guanosine diphosphate (GDP).[21] As discussed above, MTAs could be a part of an effective strategy for treating breast cancer. TNBC remains a challenging subtype of breast cancer, and there is distinct scope to address the unmet needs to improve the outcome of TNBC therapeutics. With this aim, we have used the β^{III}-tubulin-specific binding of the **NAP** peptide in demonstrating a proof-of-concept of a microtubule-specific photosensitizer (PS) for the bimodal killing of the TNBC cells using chromophore-assisted light inactivation (CALI) concept.[22,23] Specific binding of the **NAP** peptide conjugated to a substitution inert Ru(II)-polypyridyl moiety (a singlet oxygen ($^1O_2$) initiator) to the cytoskeleton protein allows this conjugate to qualify as CALI-based agent while addressing the limitations of systemic toxicity induced by conventional PDT-agents through indiscriminate intracellular reactive oxygen species (ROS) generation.[24−27] Short lifetime (~6 μs) and diffusion length (<50 nm) for $^1O_2$ in human physiology enable a highly localized spatiotemporal activity to minimize the possibility of indiscriminate systemic toxicity.[23,28−32] Importantly, literature reports suggest that CALI-based PDT agents are rarely exploited for in vivo studies.[31,32] Antibody-drug conjugates (ADCs) have also been conceived to achieve organelle/tissue-specific release of cytotoxic drugs to avoid nonspecific biodistribution and undesired systemic toxicities. However, the major shortcomings of the first- and second-generation ADCs include the immunogenic responses and fast clearance in circulation, apart from other drug-design issues.[33−37] Arguably, small molecular weight peptide-drug conjugates have the advantages of higher drug loading and enhanced tissue penetration capacity, degradation without triggering any immunogenic responses in physiology, stability toward proteolysis, and facile synthesis.[38,39] Recently, Kornienko, Bonnet, and their co-workers have demonstrated the efficacy of photoactivated chemotherapy in A549 xenografts in nude mice through the in situ release of an MT-targeting drug, rigidin.[19]

The PDT efficiency is compromised by the hypoxic feature of tumors, especially for the PDT agents that induce Type II reactions. Here, the triplet state (T_1) of the PS interacts with $^3O_2$ to form $^1O_2$, a potent ROS.[40] Therefore, combining PDT and chemotherapy is crucial to counterbalance each other's limitations.[41] Considering this, we have utilized **NAP** peptide conjugated Ru(2,2′-bipy)$_3^{2+}$ (**Rubpy**) derivative (**Ru-NAP**) as a potent bimodal chemotherapeutic and PDT agent for killing TNBC cells (Scheme 1). **Ru-NAP** conjugate is more efficient in stabilizing MT by favoring tubulin polymerization. Live cell microscopy confirms the targeting ability of **Ru-NAP** to the MT in TNBC (MDA-MB-231) cells. Thus, it causes certain toxicity in the dark through the binding of **Ru-NAP** fibers to the tubulin/MT, followed by disruption of the MT network which signifies its' chemotherapeutic effect. Moreover, in vitro and intracellular studies confirm that **Ru-NAP** also exhibits superior phototoxicity compared to the individual components, **Rubpy** or **NAP**. The higher toxicity toward live MDA-MB-231 cells accounts for the in situ generation of $^1O_2$ for inducing PDT, along with the disruption of the MT network and G2/M cell cycle arrest to induce chemotherapeutic effect. Importantly, the Hill plot supports a cooperative effect for **Ru-NAP** as a PDT agent. Control studies confirm that **Ru-NAP** is benign to normal healthy human embryo kidney (HEK293) cells under dark and light irradiation compared to MDA-MB-231 cells. The higher efficacy of **Ru-NAP** toward live MDA-MB-231 cells is also reflected in the significantly higher inhibition of tumor growth in the MDA-MB-231 tumor

Scheme 1. (a) Cartoon Representation of the Synthetic Methodology Adopted for the Synthesis of Ru-NAP, (b) Molecular Structure of Ru-NAP,and (c) Schematic Representation of Microtubule Targeted Chemotherapeutic and PDT Action Induced by Ru-NAP

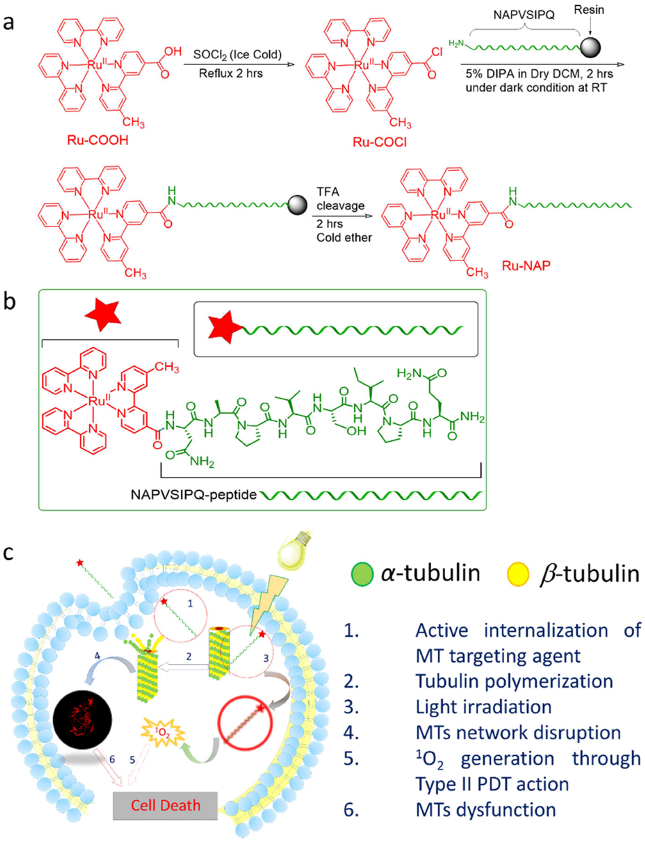

xenograft model with insignificant in vivo toxicity. This report demonstrates the proof of concept of MT-targeted and serum-stable (due to the small size and the N-stapled termini of the **NAP** peptide) PS as an effective bimodal (chemotherapeutic and PDT) agent for inhibiting tumor growth. Such examples are rather scarce in contemporary literature.[9,42−47]

■ RESULTS AND DISCUSSION

Design Strategy of Ru-NAP. Literature reports suggest that the lifetime ($T_{1/2}$) of $^1O_2$ in the cytoplasm is about 1 × 10^{-7} s with a maximum radius of reactive action of 30 nm.[39] While, at low bacterial concentrations during photodynamic inactivation of bacteria, $T_{1/2}$ for $^1O_2$ is reported to be 6 ± 2 μs with a diffusion length of <50 nm.[48] However, the efficient therapeutic performance of the Type II pathway is hindered by an insufficient supply of molecular oxygen (O_2) in the tumor microenvironment (TME) because of hypoxic tumor cells. Microtubules (MTs) are also involved in the manipulation of tumor hypoxia. Hypoxia-inducible factor 1 (HIF-1), being overexpressed in the TME regulates several target genes involved in tumor angiogenesis, matrix metabolism, apoptosis, and glycolysis leading to tumor hypoxia.[49] Tumor angiogenesis is triggered by hypoxia via activation of the HIF-1 pathway, and HIF-1 utilizes microtubules as tracks for their nuclear translocation and transcription followed by hypoxic induction. Thus, targeting and disruption of MT dynamics serve as potent barriers for tumor angiogenesis through the downregulation of the HIF-1 pathway, which is supposed to increase the efficacy of the Type II PDT agents. This motivated us to utilize the **Rubpy** derivative as an MT-targeted Type II PDT agent in the hypoxic tumor microenvironment.[43,50−53] **Rubpy** derivatives are an attractive choice as a PS primarily for the high quantum yield for a relatively long-lived transient triplet state (~100 ns) that is crucial for $^1O_2$ generation, photochemical stability, amphiphilicity, stability toward photobleaching, insignificant dark toxicity/mutagenicity and facile cellular internalization.[54,55] Importantly, the COO^--terminal tails of several acidic amino acid residues of α- and β-tubulins are located on the outer surface of MTs, and this accounts for an overall negatively charged surface. These carboxy-terminal tails, mostly of glutamate side chains on α- and β-tubulins of MTs, are the key sites of interactions for many MT-binding proteins or peptides.[56] The estimated electric field of a single MT is 52.2 electronic charges (e) per dimer.[57,58] These would further favor interaction between the cationic **Rubpy** part of **Ru-NAP**, apart from the binding of **NAP** to the MTs.

Synthesis and Characterization of Ru-NAP and the Control Molecules. With these rationales, **NAP** and **Ru-NAP** were synthesized following procedures that are elaborated in the Supporting Information. **NAP** was synthesized following the standard Hydoxybenzotriazole (HBTU) coupling protocol of the solid phase peptide synthesis (SPPS) method (Scheme S1).[59] The crude peptide was purified using reverse-phase high-performance liquid chromatography (HPLC) with C18 column and acetonitrile−water gradient, and purified **NAP** was characterized using HPLC, ^{1}H NMR, and ESI-Ms (Figures S1−S3). **Ru-NAP** was also synthesized using SPPS. First, Ru(II)-polypyridyl complex having a pendant carboxy functionality (**Ru-COOH**) was synthesized following a literature report with necessary modification in the purification process (Scheme S2).[60−63] Cis-dichlorobis(bipyridine)-ruthenium(II) (**Ru(2,2′-bipy)$_2$Cl$_2$**) and 4′-methyl-2,2′-bipyridine-4-carboxylic acid were dissolved in an ethanol−water mixture (1:1) with the addition of an equivalent amount of Na_2CO_3. The solution was allowed to reflux at 100 °C for 8 h followed by the addition of a saturated aq. solution of KPF_6 to precipitate the crude complex of **Ru-COOH**. The precipitate was purified by column chromatography and characterized using ^{1}H NMR and ESI-MS (Figures S4−S7). Then, **Ru-COOH** was converted to an acid-chloride intermediate (**Ru-COCl**) and conjugated to a **NAP** peptide-bound rink amide resin by the SPPS method.[60] This resin-attached **Ru-NAP** was further subjected to TFA cleavage and cold ether treatment to yield crude **Ru-NAP**. The crude **Ru-NAP** was purified using reverse phase HPLC (C18 column and acetonitrile−water gradient) and characterized using HPLC, ^{1}H NMR, and ESI-Ms (Schemes 1, S2 and Figures S8−S10). Pyrene is known to increase the hydrophobicity and self-assembled efficacy of the **NAP**. We also synthesized a pyrene-conjugated NAP peptide derivative (**Py-NAP**, Scheme S3) for our control studies using the SPPS method. Detailed synthetic procedures and characterization data required to ensure the desired purity of **Py-NAP** are provided in the Supporting Information. After synthesis, **Py-NAP** was purified using reverse phase HPLC (C18 column and acetonitrile−water gradient) and characterized using HPLC, ESI-Ms (Figures S11 and S12). We further synthesized 4-nitro-2,1, 3-benzoxadiazole (NBD) conjugated NAP (**NBD-NAP**; Schemes S4 and S5) for checking the aggregation inside the cell and characterized using HPLC, ^{1}H NMR, and ESI-Ms (Figures S13−S16).

Photophysical Studies of Ru-NAP. After successful synthesis, we performed the photophysical studies of the **Ru-NAP** and compared it with the commercially available PDT agent **Rubpy**. The electronic and fluorescence spectra of **Rubpy** and **Ru-NAP** were recorded. A distinct red shift in the respective absorption (461 nm, $\Delta\lambda_{Abs}$ = 7 nm) and emission (651 nm, $\Delta\lambda_{Ems}$ = 37 nm) maximum was observed for **Ru-NAP** as compared to **Rubpy** in PBS buffer (pH 7.4; Figure S17). The relative emission quantum yield ($\Phi_{Em}{}^{Ru\text{-}NAP}$) for **Ru-NAP** was evaluated as 0.70 (**Rubpy** as a reference) in deionized water, saturated with O_2 (Figure S18). Considering the substitution of one 2,2′-bipy with **NAP** functionalized 2,2′-bipy through an amide linkage in **Ru-NAP**, these redshifts are anticipated. Luminescence lifetimes of the **Ru-NAP** (291.7 ± 1.002 ns) and **Rubpy** (366 ± 1.42 ns) using λ_{Ex} = 450 nm; $\lambda_{Em}{}^{Ru\text{-}NAP}$ = 651 nm and $\lambda_{Em}{}^{Rubpy}$ = 614 nm in aq. PBS buffer (pH = 7.4) at room temperature (RT) was evaluated (Figure S19 and Table S1). Typically, such molecules with an extended luminescence lifetime are better suited for use as a PDT agent.[26,64−67]

Docking and Simulations Studies. We performed docking studies to check the validity of our design rationale and also to understand the possible binding site for **Ru-NAP** to the tubulin dimer. Both **NAP** and **Ru-NAP** showed thermodynamically favorable binding interactions with tubulin, as reflected in the negative binding free energies (Tables S2−S4). The average binding energy values obtained for **NAP** and **Ru-NAP** are −6.77 ± 0.61 and −8.28 ± 0.87 kcal/mol, respectively. A paired t-test showed significantly lower binding energy for **Ru-NAP** than for **NAP** (p-value: 0.000091). The dissociation constant (K_D) obtained for **Ru-NAP** is 1 order of magnitude lower than that for **NAP** suggesting higher affinity (K_a) binding for **Ru-NAP**. The respective binding constants of **NAP** and **Ru-NAP** are found to be 9.24 × 10^4 and 1.19 × 10^6 M^{-1} showing higher binding of **Ru-NAP** compared to **NAP** (Table S5). Blind docking of **NAP** and **Ru-NAP** on the tubulin

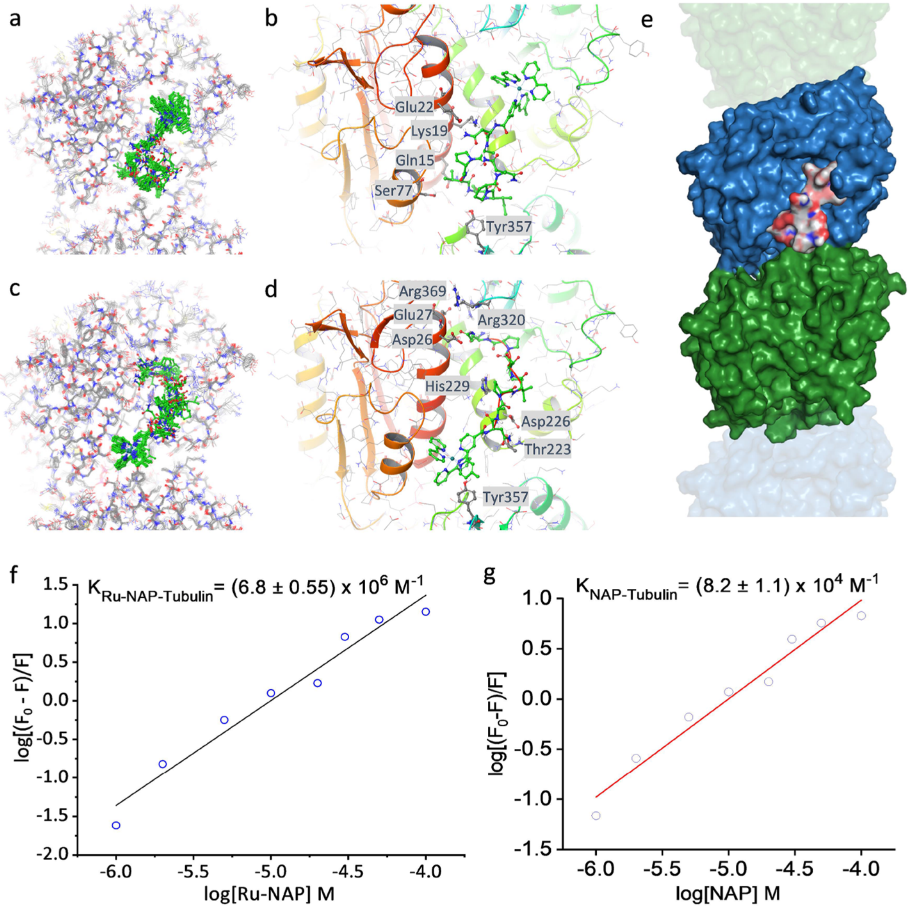

Figure 1. Binding interaction of Ru-NAP with tubulin. (a) Tubulin-**Ru-NAP** complex **1**. Snapshots from the MD simulation are superimposed. **Ru-NAP** is shown in green. (b) Close-up view of the last frame of the MD trajectory with interacting residues is highlighted. (c) Tubulin-**Ru-NAP** complex **2**. (d) Interacting residues. (e) Surface representation shows binding of **Ru-NAP** (pink) on β-tubulin (blue). The α-subunit is shown in green. Binding constant curves of (f) tubulin and **Ru-NAP** and (g) tubulin and **NAP** from the study of quenching of tryptophan fluorescence of tubulin in the presence of different concentrations (1−100 μM) of **Ru-NAP** or **NAP** in BRB80 buffer (80 mM PIPES, 1 mM EGTA, 1 mM $MgCl_2$, pH 6.9) at 25 °C.

dimers showed potential binding sites including the taxol binding sites, as depicted in Figure S20. Further targeted docking to the taxol binding site on β-tubulin produced low-energy binding modes (Table S4 and Figure S21). Computational studies suggest two low-energy binding modes of **Ru-NAP**: Ru-head is bound to the taxol binding site (**Ru-NAP** complex **1**) and the peptide tail is bound to the taxol binding site (**Ru-NAP** complex **2**). Previous literature also suggests the binding of the NAP-peptide to the taxol binding site.[68] MD simulations showed very stable binding of **NAP** as well as **Ru-NAP** with tubulin throughout the simulation time (Figure S22). Figure 1a−e shows a snapshot of MD simulation for the **Ru-NAP** and tubulin complexes in two possible binding conformations. RMSD profiles of the MD simulations, interacting residues with interaction fractions, and the schematics of the interactions are shown in Figures S23−S31. Water plays an important role in the binding interaction of the peptide, as evident from the several water bridges formed during the MD simulation (Figures S26−S31). It was also observed that the bipyridyl moieties of the **Ru-NAP** headgroup may interact with the tyrosine side chains by forming pi-stacking interactions (Figures 1a−e and S31). The role of the cationic Ru(II)-polypyridyl moiety is important in the binding of **Ru-NAP** with tubulin as tubulin remains highly negatively charged at neutral pH. Charges on tubulin alpha and beta chains are −12 each; therefore, the contribution of long-range electrostatic interaction with the cationic Ru(II)-core of the Ru(II)-polypyridyl moiety significantly drives this bimolecular association (Tables S6 and S7).

Binding of Ru-NAP with Tubulin. The binding of **NAP** or **Ru-NAP** to tubulin was evaluated following a conventional luminescence quenching process of tryptophan (Trp) of tubulin as a function of [**NAP**] or [**Ru-NAP**].[69−72] Decrease in intrinsic tryptophan fluorescence of tubulin upon binding of **NAP** or **Ru-NAP** with tubulin indicates that their binding causes perturbation of tubulin conformation in the vicinity of tryptophan residues (Figure 1f, g). The linearity of the Stern−Volmer plot confirms the dynamic quenching process, while the experimental data show a much higher binding between **Ru-NAP** and tubulin ($K_a^{\text{Ru-NAP-tubulin}}$ = (6.8 ± 0.55) × 10^6 M^{-1}), as compared to **NAP** and tubulin ($K_a^{\text{NAP-tubulin}}$ = (8.2 ± 1.1) × 10^4 M^{-1}). This also agrees well with the results of the docking studies. This further corroborates our proposition that the cationic Ru(II)-polypyridyl moiety in **Ru-NAP** favors a stronger binding to β-tubulin than **NAP**.

Ru-NAP Forms Fibrillar Aggregates. **NAP** peptide is known to form fibrillar structures when incubated for 7 days.[73,74] We studied the morphology of **NAP**, **Py-NAP**, and **Ru-NAP** after incubation for 5 days in aq 1× PBS buffer using transmission electron microscopy (TEM). **NAP** forms the

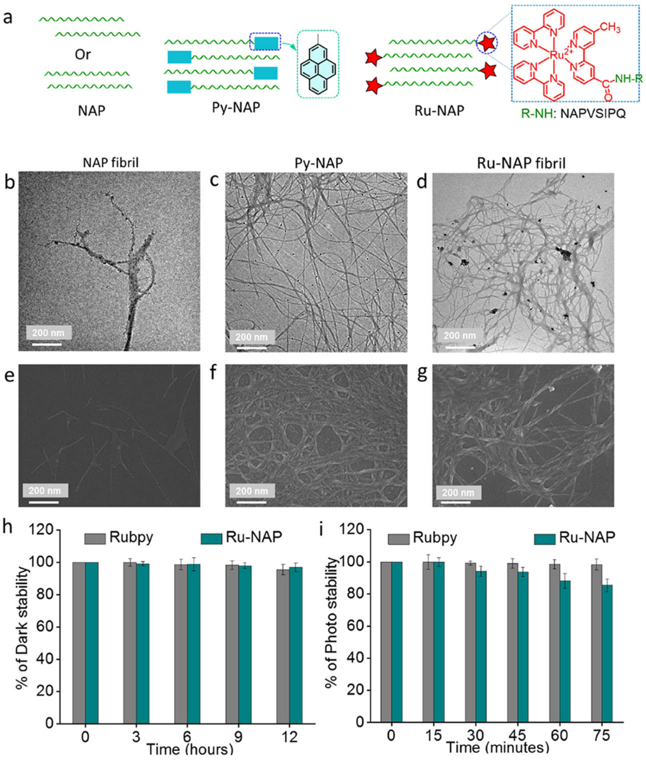

Figure 2. (a) Schematic representation of the self-assembly of **NAP**, **Py-NAP** and **Ru-NAP**. TEM images of (b) **NAP** (100 μM; 1× PBS buffer (pH = 7.4), while (e) represents the corresponding SEM image. (c) TEM image of **Py-NAP** (100 μM; 1× PBS buffer (pH = 7.4) containing 2.5% DMSO (v/v), while (f) represents the corresponding SEM image. (d) TEM image of **Ru-NAP** (100 μM; 1× PBS buffer (pH = 7.4) containing 2.5% DMSO (v/v), while (g) represents the corresponding SEM image. (h) Dark stability of **Rubpy** and **Ru-NAP** using 75 μM of each of these complexes in 1× PBS buffer (pH = 7.4) containing 1% DMSO (v/v). Absorbances were recorded in 3 h intervals up to 12 h. (i) Photo stability of **Rubpy** and **Ru-NAP** using 75 μM of each of these complexes in 1× PBS buffer (pH = 7.4) containing 1% DMSO (v/v). Absorbance was recorded after irradiation for 1 min with 450 nm laser light (200 mW·cm^{-2}; 1 min, 12 J·cm^{-2}) in 15 min intervals up to 75 min. The ±SD was calculated from three independent sets of experiments.

fibrillar structure as previously reported (Figure 2a,b). TEM images recorded for **Py-NAP** also showed fiber-like morphology (Figure 2c). Better fiber formation for **Py-NAP**, compared to **NAP** under identical conditions, could be ascribed to the ability of the Py moiety to participate in cation−π/π−π stacking interactions. Importantly, the degree of fiber formation was more extensive for **Ru-NAP**, as compared to **NAP** or **Py-NAP** (Figure 2d). Literature reports suggest that the cationic Fe^{II}(2,2′-bipy)$_3^{2+}$ moiety in Fe^{II}(2,2′-bipy)$_3^{2+}$-collagen conjugate favors the self-assembly process and fiber formation.[75] A similar phenomenon was observed in the present study. Importantly, the extent of fiber formation for **Py-NAP** was lower than that of **Ru-NAP** when both were subjected to self-assembly to form fibers under identical conditions. This presumably arises from a head-to-tail orientation of the **Ru-NAP** molecules during the self-assembly process for fiber formation (Figure 2a). The self-assembly behavior of **NAP**, **Py-NAP**, and **Ru-NAP** was further confirmed using scanning electron microscopy (SEM). The SEM images for **NAP** show short fiber formation (Figure 2e), which is found to be improved in the case of **Py-NAP** and **Ru-NAP** (Figure 2f,g). Figure S32 shows the histogram of the average diameter of the **NAP**, **Py-NAP**, and **Ru-NAP** fibers. These indicate that **Rubpy** favored the self-assembly process in **Ru-NAP**.

Dark Stability and Photostability of Ru-NAP. We investigated the dark and photostability of the **Ru-NAP** and compared these with **Rubpy**. Both complexes showed insignificant degradation in the dark when incubated in 1× PBS buffer (pH 7.4) for 12 h (Figures 2h and S33). The stability of **Rubpy** and **Ru-NAP** after successive irradiation with a 450 nm laser (200 mW·cm^{-2}, 1 min, 12 J·cm^{-2}) in 1× PBS buffer (pH 7.4) was examined (ESI). Only insignificant bleaching was observed for **Rubpy**, while a slight degradation (<7%) was observed for **Ru-NAP** due to photobleaching even after 5 cycles (Figures 2i and S33). This ensured that the conjugation of **NAP** to **Rubpy** in **Ru-NAP** had no influence on its dark stability, while a marginal decrease in its photostability characteristics was observed.

Type II ROS Generation of Ru-NAP. To investigate the efficacy of **Ru-NAP** in generating $^1O_2$, we performed the 1,3-diphenylisobenzofuran (DPBF) assay in Milli-Q water containing 1% DMSO (v/v). The absorbance of DPBF was found to decrease gradually when DPBF was irradiated for 15 s in the presence of **Ru-NAP** with a 450 nm laser (Figures 3a and S34a,b). However, the absorbance of DPBF remained unaltered when identical experiments were performed without any 450 nm irradiation. This confirmed the in situ ROS generation on irradiation of **Ru-NAP** at 450 nm. The DPBF assay is used for the detection of $^1O_2$, apart from other ROS species.[76] To reconfirm the in situ generation of $^1O_2$ as a transient species, we further performed an additional 9,10-anthracenediyl-bis(methylene)dimalonic acid (ABDA) assay, which is specific for $^1O_2$.[77] A successive decrease in the absorbance of ABDA was observed after irradiation with 450 nm light in the presence of **Ru-NAP** in Milli-Q water. The reaction of ABDA with $^1O_2$, generated in situ, on irradiation of **Ru-NAP**, accounted for this observed gradual decrease in absorbance (Figures 3b and S34c,d). However, control experiments revealed that the absorbance of ABDA remained unaltered for **Ru-NAP** treated solution without photo irradiation. This further corroborated our presumption that **Ru-NAP** belonged to the Type II PDT agent. The DPBF and ABDA assays for **Rubpy** also confirm $^1O_2$ generation but to a lesser extent than **Ru-NAP** (Figure S35). The quantum yield for $^1O_2$ generation (Δ^1O_2) for **Ru-NAP** was evaluated as 0.55 by UV−vis titration studies of DPBF using methylene blue (MB) as a reference (Figure S36). This is a reasonably high value because we used Milli-Q water medium saturated with O_2 and is higher than the desired value (Δ^1O_2 = 0.5) for any PDT applications.[78] These data confirmed the therapeutic potential of Ru-NAP on irradiation with 450 nm light. Next, the possibility of the generation of Type I ROS (hydroxyl radical ($^\bullet$OH) or/and superoxide radical ($O_2^{\bullet-}$)) as a transient species on irradiation of **Ru-NAP** with 450 nm light was examined. Typical terephthalic acid (TPA) and 5,5′-dimethyl-1-pyrroline N-oxide (DMPO)-based assays were performed respectively to identify the formation of transient ROS species like $^\bullet$OH and $O_2^{\bullet-}$ on irradiation of **Ru-NAP** with 450 nm light (Figure S37, ESI). These results confirm that **Ru-NAP** failed to induce the formation of Type I PDT under the experimental conditions.[79,80]

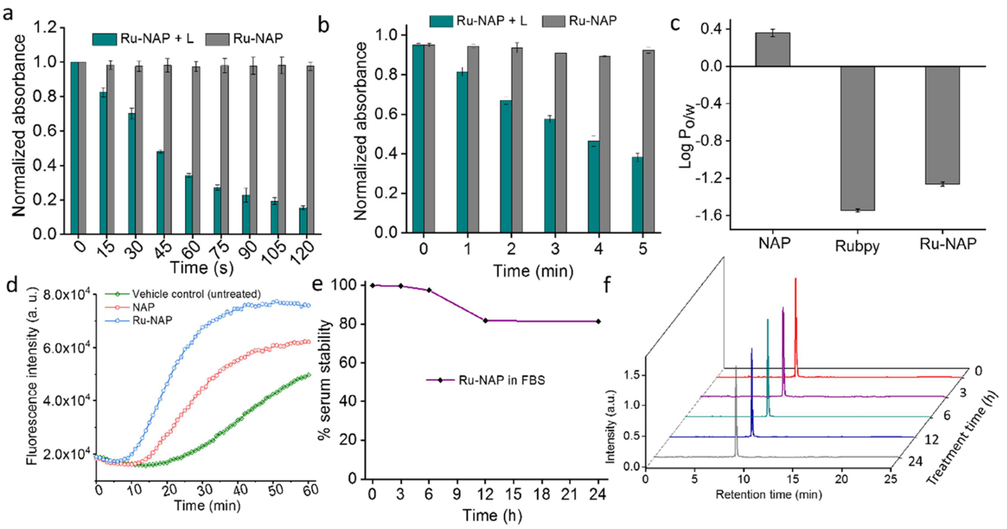

Figure 3. (a) Changes in absorbance of DPBF treated with **Ru-NAP** ([DPBF] = 125 μM and [**Ru-NAP**] = 2.5 μM in Milli-Q water containing 1% DMSO (v/v)) were recorded at 419 nm following irradiation with 450 nm light (200 mW·cm^{-2}, 15 s, 3 J·cm^{-2}). (b) Changes in absorbance of [ABDA] (80 μM) treated with [**Ru-NAP**] (1.6 μM) in Milli-Q water under irradiation of 450 nm light (200 mW·cm^{-2}, 1 min, 12 J·cm^{-2}). (c) Determination of lipophilicity of **NAP**, **Rubpy** and **Ru-NAP** by the shake-flask method using an equal mixture of an octanol—water mixture. The lipophilicity of **Ru-NAP** was found to be increased compared to the **Rubpy**. (d) Fluorescence-based tubulin polymerization assay of **NAP** and **Ru-NAP** using the fluorescence-based tubulin polymerization assay (Cat. # BK011P) from Cytoskeleton. (e) Stability of **Ru-NAP** (%) and (f) time-dependent HPLC of **Ru-NAP** in fetal bovine serum (FBS, 20% v/v in 1× PBS buffer (pH = 7.4)) up to 24 h. The HPLC analysis of the **Ru-NAP** (100 μM) incubated sample in 20% FBS showed >80% stability up to 24 h.

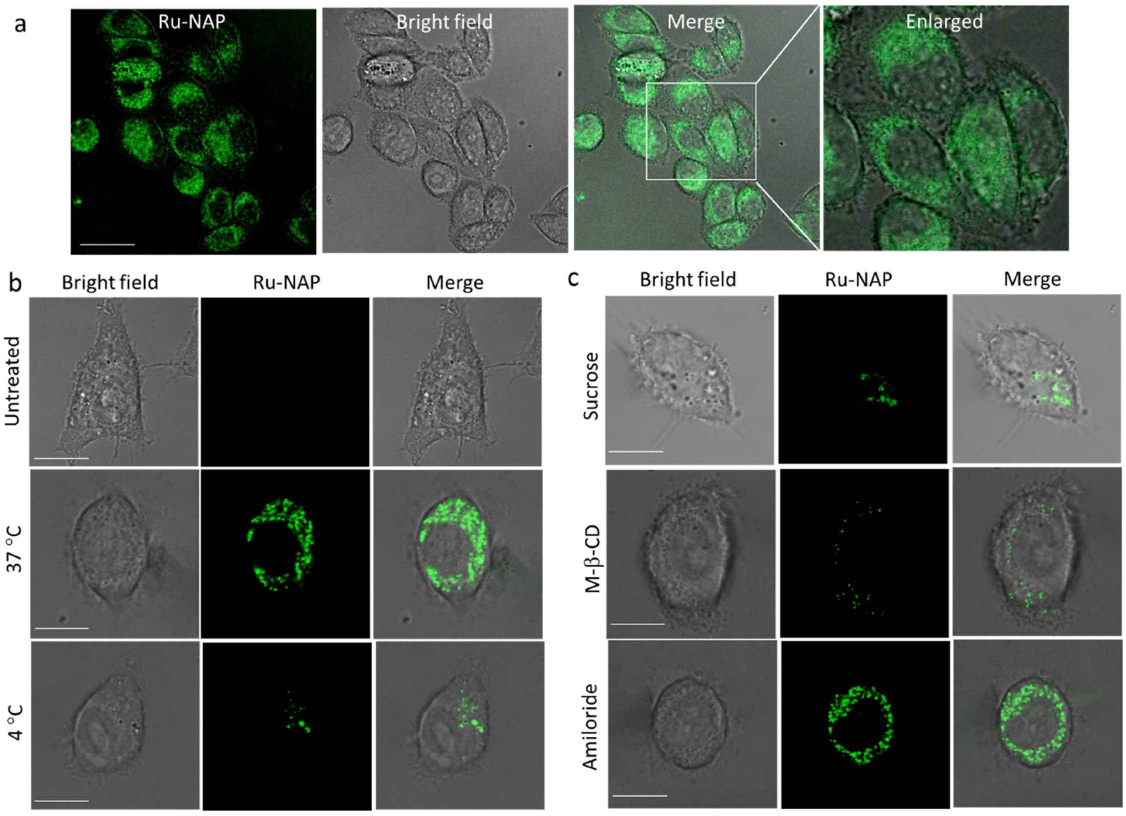

Figure 4. Representative CLSFM images showing accumulation of **Ru-NAP** (**Ru-NAP** shows intrinsic green fluorescence) in live MDA-MB-231 cells (a) incubated with **Ru-NAP** (5 μM for 4 h; scale bar, 5 μm) at 37 °C, (b) untreated (upper row) and incubated with 5 μM **Ru-NAP** for 4 h at 37 °C (middle row) or 4 °C (bottom row), and (c) preincubated with 400 mM sucrose for 30 min (upper row) or 10 mM M-β-CD for 30 min (middle row) or 3 mM amiloride for 15 min (bottom row).

Lipophilicity Measurement of Ru-NAP. Appropriate lipophilic balance rather than the overall charge of the compound is an important parameter for effective cellular internalization. Lipophilicity takes care of the solvation ability of molecules in fats and lipids as well as in aqueous media. It can be correlated with cellular internalization and up-

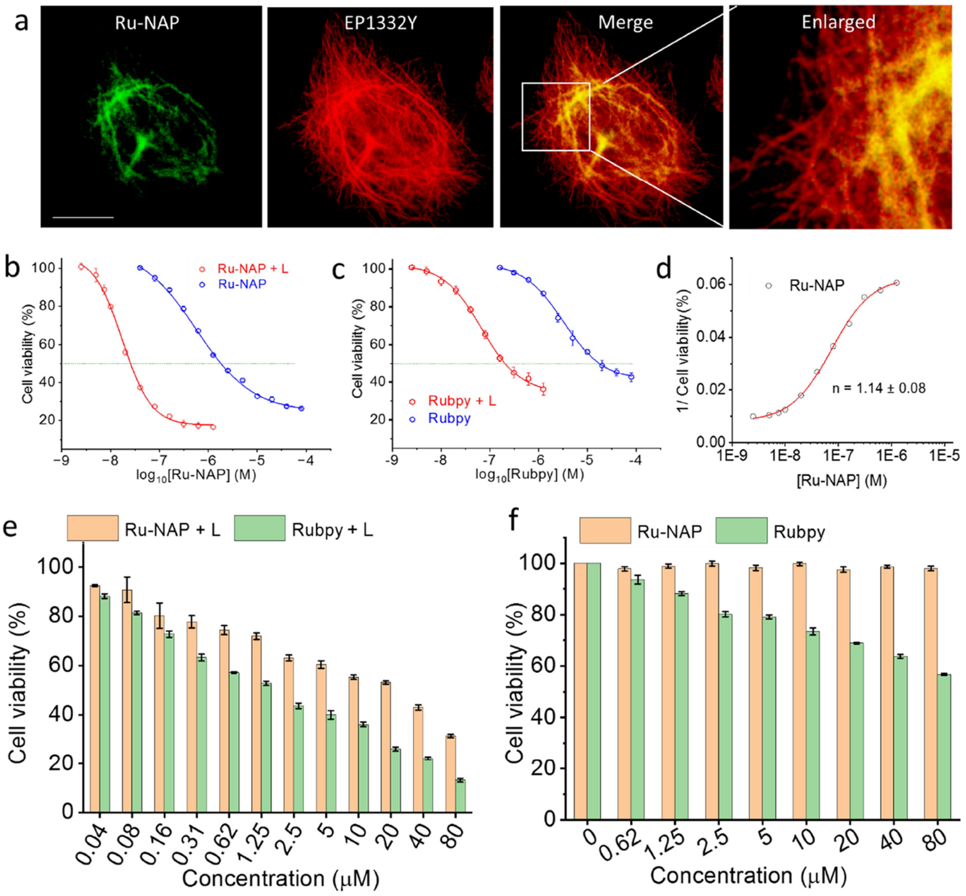

Figure 5. (a) Representative CLSFM images showing colocalization of **Ru-NAP** (20 μM for 4 h; intrinsic green fluorescence) with MT (red fluorescence). Co-localization is shown in the merged image. Merged image indicates the nice colocalization of **Ru-NAP** with the MT (Pearson's coefficient: 0.88). Dose−response profiles of (b) **Ru-NAP** under dark and after light irradiation (450 nm, 200 mW·cm^{-2}, 5 min, 60 J·cm^{-2}) and (c) **Rubpy** under dark and after light irradiation (450 nm, 200 mW·cm^{-2}, 5 min, 60 J·cm^{-2}) from the toxicity data using the MTT assay. (d) Hill plot of the toxicity data of the **Ru-NAP** followed light treatment. (e) Cell cytotoxicity of the **Ru-NAP** and **Rubpy** was measured using the MTT assay after light irradiation (450 nm, 200 mW·cm^{-2}, 5 min, 60 J·cm^{-2}) in HEK293 cells. (f) Dark toxicity of **Ru-NAP** and **Rubpy** in HEK293 cells.

take.[54,81,82] The distribution coefficients (log *P*) of **NAP**, **Rubpy**, and **Ru-NAP** were evaluated in an octanol−water mixture using the shake-flask method. The evaluated lipophilicity of **Ru-NAP** was higher than that of **Rubpy** (Figures 3c and S38). Higher lipophilicity improves the cellular internalization process and helps to overcome accumulation defects with consequential cytotoxicity.[83,84]

Effect of Ru-NAP on Tubulin Dynamics, Buffer, and Serum Stability of Ru-NAP. A literature report suggests that **NAP** interacts with MT end-binding proteins (EB1 and EB3) and increases the dendritic spine density.[85] We examined the binding of the **Ru-NAP** to the tubulin and its' influence on the tubulin polymerization process using a fluorescence-based tubulin polymerization assay (BK006P). The extent of the light scattered by MT is proportional to the concentration of the microtubule polymer. A plot of the extent of light scattered as a function of the time yielded the polymerization curve depicting the nucleation, growth, and steady-state equilibrium (Figure 3d). It is evident from Figure 3d that **Ru-NAP** is more efficient in stabilizing the microtubule and enhances tubulin polymerization in comparison to **NAP** (used in equimolar concentration), which was used as a positive control. Next, we checked the stability of **Ru-NAP** in 1× PBS buffer (pH = 7.4) and fetal bovine serum (FBS, 20% v/v in 1× PBS buffer (pH = 7.4)) up to 24 h. The HPLC analysis of the Ru-NAP (100 μM) incubated sample in both PBS and 20% FBS showed >95 and >80% stability, respectively, until 24 h due to the small size and the N-stapled termini of the **NAP** peptide (Figures 3e,f and S39).

Cellular Uptake of Ru-NAP. **NAP** is known to be a cell-penetrating peptide. As discussed earlier, presumably, the endocytosis pathway rather than membrane translocation prevailed at the low concentration used for our studies at physiological conditions.[86] We checked the morphology of **Ru-NAP** in an RPMI medium supplemented with 10% fetal bovine serum used for the cell culture. The TEM and SEM images of **Ru-NAP** also show the fiber formation (Figure S40). Next, we investigated the effective cellular uptake of **Ru-NAP** using high-resolution live cell confocal laser scanning fluorescence microscopy (CLSFM) imaging in the MDA-MB-231 cell. The MDA-MB-231 cell line is ER, PR, and E-cadherin negative and expresses mutated p53. These cells also lack the growth factor receptor HER2 and represent a good model of triple-negative breast cancer.[87] Four hours post-treatment was found to be adequate for the internalization of **Ru-NAP** (5 μM) into the cellular cytoplasm (Figure 4a; see merged image with bright field). We further checked the cellular uptake of **Ru-NAP** in MDA-MB-231 and HEK293 cells using inductively coupled plasma-mass spectrometry (ICP-MS). The result shows a ∼2.6-fold higher accumulation of **Ru-NAP** in live MDA-MB-

231 cells compared to that of live HEK293 cells (Figure S41). We have performed new live cell CLSFM by incubating live MDA-MB-231 cells with **Ru-NAP** at 37 and 4 °C to examine active or passive uptake of the drug. Interestingly, we observed a 90% reduction in **Ru-NAP** Mean Fluorescence Intensity (MFI) inside cells at 4 °C compared to 37 °C suggesting an energy-dependent uptake of **Ru-NAP** in live MDA-MB-231 cells through the endocytosis process (Figures 4b and S42). This indicates the active cellular internalization of **Ru-NAP**. To further confirm the role of endocytosis for the **Ru-NAP** uptake inside cells, we have applied a range of endocytosis inhibitors, namely, sucrose (Clathrin endocytic inhibitor), methyl-β-Cyclodextrin (M-β-CD; caveolin endocytic inhibitor), and amiloride (macropinocytosis inhibitor). CLSFM data indicate a significant reduction in **Ru-NAP** uptake ($p < 0.001$) in cells following pretreatment with sucrose (Figures 4c and S42). MDA-MB-231 cells pretreated with M-β-CD (caveolin endocytic inhibitor) also show a 5-fold reduction in cellular uptake of **Ru-NAP**. However, pretreatment with amiloride showed insignificant changes in **Ru-NAP** cellular uptake under similar conditions. These results indicate that clathrin- and caveolin-dependent endocytic processes are involved in the uptake of **Ru-NAP** in MDA-MB-231 cells. To ascertain the molecular aggregate inside the live MDA-MB-231 cells, we further used fluorescence imaging studies using **NBD-NAP**. Being an environmentally sensitive fluorophore, NBD is frequently used to ascertain the formation of molecular assembly(ies) in the cellular milieu. NBD derivatives typically show strong fluorescence as they get readily partitioned into hydrophobic pockets and this is accompanied by a characteristic green NBD fluorescence maximum (λ_{Em} = 540 nm) following excitation at 470 nm.[88] Internalization of **NBD-NAP** with subsequent partitioning within the fibrillar aggregates in live MDA-MB-231 showed a strong green fluorescence to confirm the significant fiber of **NBD-NAP** (Figure S43). However, such a fiber is less prominent in HEK293 cells due to less cellular uptake compared to MDA-MB-231 cells (Figure S44). This supports our presumption of intracellular fibers of analogous molecules of **Ru-NAP**.

Co-Localization of Ru-NAP with Tubulin/MT. To verify if **Ru-NAP** was localized on the MTs, we incubated MDA-MB-231 cells with **Ru-NAP** (20 μM for 4 h), costained them with the microtubule-specific marker (EP1332Y), and analyzed them via CLSFM (Figure 5a). Significant colocalization of **Ru-NAP** with tubulin was detected, suggesting a strong association of **Ru-NAP** with MTs. A detailed plot profile analysis demonstrates significant colocalization of the green-colored **Ru-NAP** and red-colored tubulin (Figure S45). Co-localization analysis of **Ru-NAP** (green) with tubulin (red) showed a Pearson Coefficient (R) of 0.88. This seems rational considering the improved lipophilicity and higher surface charge affinity for **Ru-NAP** as compared to **NAP**, which is otherwise known to bind preferentially to β-tubulin. These contributed to the higher evaluated binding constants for **Ru-NAP** compared to **NAP** (control) toward β-tubulin and confirmed the high targeting ability of the **Ru-NAP** to MT in live MDA-MB-231 cells.

Cytotoxicity Study of Ru-NAP. MT serves as "freeways" for intracellular trafficking. Such fiber formation on the MT surface and/or inside the tubular structure of MT would further interfere with the intracellular trafficking of vesicles and organelles, transport of cargo by motor proteins from the kinesin/dynein superfamilies and ion transport, apart from binding to many MT-binding proteins, which collectively have a serious implication on cellular motility and cell death.[56,89] Therefore, we assessed the dark toxicity (chemotherapeutic effect) of the **Ru-NAP** in MDA-MB-231 cells for 24 h using the MTT assay. **Ru-NAP** shows certain cytotoxicity in the dark and the corresponding IC_{50} value is 2.9 ± 0.5 μM indicating the significant chemotherapeutic effect of the **Ru-NAP** due to the binding of the **Ru-NAP** fibers to the tubulin/MT of the MDA-MB-231 cells (Figure 5b). The dark toxicity of the **Ru-NAP** is much higher than that of **Rubpy** (IC_{50} of **Rubpy** under dark is 21.1 ± 4.2 μM; Figure 5c). Next, we assessed the PDT efficacy of the **Ru-NAP** and compared the same with the **Rubpy** as the control. The MDA-MB-231 cells were incubated with varying concentrations of **Ru-NAP** and **Rubpy** for 4 h followed by light irradiation (450 nm, 200 $\mathrm{mW{\cdot}cm^{-2}}$, 5 min, 60 $\mathrm{J{\cdot}cm^{-2}}$) and further kept in the dark for another 24 h. The cytotoxicity data revealed that **Ru-NAP** showed significant light toxicity to the MDA-MB-231 cells with a ${}^{\mathrm{Light}}\mathrm{IC}_{50}{}^{\mathrm{Ru\text{-}NAP}}$ value of 32.5 ± 7.8 nM, a value that is ~89 times lower than **Ru-NAP** (${}^{\mathrm{Dark}}\mathrm{IC}_{50}{}^{\mathrm{Ru\text{-}NAP}}$ = 2.9 ± 0.5 μM, Figure 5b) due to its combined effect of chemotherapeutic through the induction of higher MT polymerization and PDT. It is noteworthy that **Rubpy** shows certain cytotoxicity in the dark and upon light irradiation. The IC_{50} of dark toxicity of **Rubpy** [${}^{\mathrm{Dark}}\mathrm{IC}_{50}{}^{\mathrm{Rubpy}}$] is 21.1 ± 4.24 μM and the IC_{50} of light toxicity of **Rubpy** ${}^{\mathrm{Light}}\mathrm{IC}_{50}{}^{\mathrm{Rubpy}}$ (0.24 ± 0.05 μM; Figure 5c). Most importantly, ${}^{\mathrm{Dark}}\mathrm{IC}_{50}{}^{\mathrm{Ru\text{-}NAP}}$ (2.9 μM) is lower by ~7.2 times and ${}^{\mathrm{Light}}\mathrm{IC}_{50}{}^{\mathrm{Ru\text{-}NAP}}$ value is lower by ~7.3 times than that for ${}^{\mathrm{Dark}}\mathrm{IC}_{50}{}^{\mathrm{Rubpy}}$ (21.1 μM) and ${}^{\mathrm{Light}}\mathrm{IC}_{50}{}^{\mathrm{Rubpy}}$ (0.24 μM) respectively. Thus, these data reveal that **Ru-NAP** is more cytotoxic than **Rubpy** due to its' chemotherapeutic effect and **Ru-NAP** on light irradiation shows a substantially low IC_{50} value of 32.5 nM toward live MDA-MB-231 cancer cells (Figure 5b,c, Table S8).[55] The **NAP** peptide alone did not show light or dark toxicity toward live MDA-MB-231 cells up to 200 μM concentration and this agreed well with the literature reports (Figure S46).[36] To check the PDT effect of **Ru-NAP** in nontumorigenic normal human embryo kidney cells (HEK293) cells, these cells were incubated with varying concentrations of **Ru-NAP** for 4 h in the dark. These pretreated cells were then irradiated for 5 min (450 nm, 200 $\mathrm{mW{\cdot}cm^{-2}}$, 5 min, 60 $\mathrm{J{\cdot}cm^{-2}}$) and kept in the dark for another 24 h. It showed a much lower toxicity toward HEK293 cells (${}^{\mathrm{Light}}\mathrm{IC}_{50}{}^{\mathrm{Ru\text{-}NAP}}$[HEK293] 17.2 ± 2.5 μM; Figure 5e) compared to MDA-MB-231 cells (${}^{\mathrm{Light}}\mathrm{IC}_{50}{}^{\mathrm{Ru\text{-}NAP}}$ value of 32.5 nM). Importantly, **Ru-NAP** under dark incubation for 24 h did not show detectable toxicity up to 80 μM toward HEK293 cells (Figure 5f). However, **Rubpy** shows significant dark and light toxicity to the HEK293 cells (Figure 5e,f). The **NAP** peptide alone did not show light or dark toxicity up to 200 μM concentration toward live HEK293 cells (Figure S47). We further checked the phototoxicity of the **Ru-NAP** after irradiation with green light (520 nm) and red light (630 nm), apart from the blue light (450 nm). Irradiation with red light shows insignificant phototoxicity (IC_{50} is similar to that of dark toxicity), while this is most prominent when blue light (450 nm) is used (Figure S48b and Table S8). Irradiation with green light shows a slightly lower PDT effect compared to the one observed with blue light (Figure S48a and Table S8). The minimal PDT effect of red light compared to the green light and blue light correlates well with the relative difference in the molar absorptivity of **Ru-NAP** in the respective spectral zone.

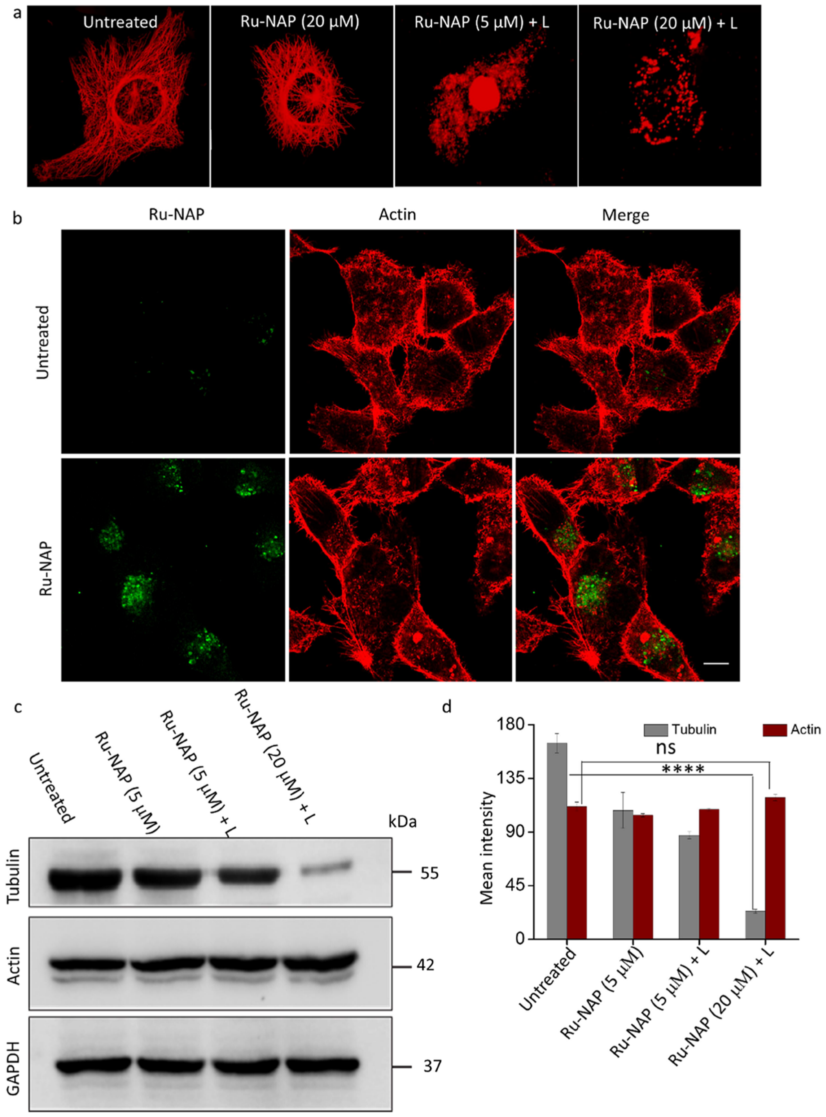

Figure 6. (a) Effect of **Ru-NAP** on the MT/tubulin network in live MDA-MB-231 was studied using CLSFM. A significant disruption of the MT network of the live MDA-MB-231 cells was evident for **Ru-NAP** treatment both under dark and with light irradiation (450 nm, 200 mW·cm^{-2}, 5 min, 60 J·cm^{-2}). (b) Effect of **Ru-NAP** on the Actin network (stained using Alexa Fluor 568 Phalloidin) in live MDA-MB-231 was studied in CLSFM. There is no change in the Actin network of the live MDA-MB-231 cells for **Ru-NAP** (20 μM, 4 h) treatment. (c) Representative Western blots for tubulin, actin, and GAPDH in MDA-MB-231 cells; either untreated or treated with **Ru-NAP** (5 or 20 μM) for 4 h with or without blue light photoactivation. GAPDH is shown as the loading control. The migration of protein molecular weight markers is indicated on the right. (d) Densitometry analysis represents the fold change in tubulin, and actin, normalized to GAPDH (error bars represent means ± SEM). Asterisks denote statistically significant differences (***$P < 0.001$, t test).

We further studied the dark toxicity and phototoxicity of the **Ru-NAP** under blue light irradiation in human cervical cancer (HeLa) cells and human breast cancer (MCF7) cells. **Ru-NAP** showed similar dark and phototoxicity to that of MDA-MB-231 cells (Figure S49). Table S8 reveals the IC_{50} value of **Ru-NAP** and **Rubpy** in different cancer and normal cells, along with their respective phototoxic index (PI; IC_{50} under dark/IC_{50} under light irradiation). The observed high toxicity of **Ru-NAP** in MDA-MB-231 cells compared to HEK293 cells presumably lies in the accelerated metabolic rate of MDA-MB-231 cells as a result of the Warburg effect and the tendency of small molecules to accumulate in cells once they have formed aggregates as in the case of **Ru-NAP**.[90−92] We utilized live-cell high-resolution CLSFM to test the uptake of **Ru-NAP** (5 μM for 4 h) in MDA-MB-231 cells in the ATP-depleted M1 medium supplemented with 10 mM sodium azide and 10 mM 2-deoxy-D-Glucose (inhibitor of glycolysis), allowing us to investigate the Warburg effect. The Mean Fluorescence Intensity (MFI) of **Ru-NAP** decreased ∼5 fold in the presence 2-deoxy-D-glucose which indicates a 5-fold reduction in the drug uptake into cancer cells in the presence of glycolysis inhibitors and provides direct evidence for the operation of the Warburg-phenomenon-dependent **Ru-NAP** cellular uptake (Figure S50). Thus, the above results reveal that the conjugation of **NAP** to **Rubpy** has a profound effect in reducing the IC_{50} of MDA-MB-231 cells compared to two individual candidates (**NAP** and **Rubpy**). These indicate the potentiality of **Ru-NAP** as a bimodal PDT agent compared to **Rubpy** due to the microtubule targeting ability, fiber formation, and PDT effect. It is worth mentioning here the IC_{50}^{Light} of various derivatives (with small organic molecules) of Ru(II)-polypyridyl complexes toward various live cancer cells are typically >5 μM and considering these, the observed IC_{50}^{Light} (32.5 nM) of **Ru-NAP** is significant.[27,55,93] The cell viability vs log[**Ru-NAP**] under light irradiation plot, a dose–response plot, is sigmoidal (Figure 5b) in nature. It has been established that the sigmoidal plots are better than linear ones for explaining the dose-dependent drug efficacy[94] as this demonstrates the β-tubulin-specific **Ru-NAP** induces a cooperative influence as obtained from the Hill plot (n = 1.14) in terms of cellular killing by $^1O_2$ and chemo toxic effect of **Ru-NAP** fibers (Figure 5d). $n > 1$ in the Hill plot indicates the cooperative influence. Next, we performed the dark and phototoxicity studies of **Ru-NAP** under hypoxia (1% O_2) to confirm the role of MT targeting in the management of tumor hypoxia. It shows similar toxicity as in normoxia (21% O_2), which indicates that the MT targeting is beneficial for **Ru-NAP** as a potential Type II PDT agent (Figure S51). Table S8 indicates the corresponding IC_{50} and PI of **Ru-NAP** in hypoxia and normoxia.

Immunocytochemistry for the Investigation the Effect of Ru-NAP on the MT/Tubulin Network. The high targeting ability of the MTs and the significant PDT efficacy of **Ru-NAP** motivated us to examine the mechanistic pathway for cell death. MTs comprise α and β-tubulin heterodimers that undergo dynamic cycles of polymerization and depolymerization processes. A dynamic balance ensures proper cellular functions and survival.[12] To test the dynamics of the MT network following the treatment with **Ru-NAP** and then photoactivation, we performed immunocytochemistry with anti-tubulin antibody in live MDA-MB-231 cells exposed to **Ru-NAP**. Without photoactivation, **Ru-NAP** treatment (20 μM for 4 h) had a significant impact on the MT network, indicating perturbation in structural integrity due to the binding of the **Ru-NAP** fibers to MT, which accounts for its chemotherapeutic effect under dark (Figure 6a). Moreover, analogous experiments with light activation showed a more significant dose-dependent disruption of the MT network, suggesting an imbalance in the polymerization-depolymerization cycle. This agreed well with the fluorescence-based tubulin polymerization assay showing enhanced tubulin polymerization in the presence of **Ru-NAP**. As a part of the detailed mechanism studies, we checked the effect of **Ru-NAP** on the Actin network of MDA-MB-231 cells. There is no change in the actin network of the live MDA-MB-231 cells treated with 20 μM **Ru-NAP** (Figure 6b). Moreover, there is no colocalization of the **Ru-NAP** with the actin network, indicating the precise targeting of the **Ru-NAP** to the tubulin/MT (Figure 6b). To further validate the tubulin-specific binding/activity of **Ru-NAP**, which promotes specific degradation of the tubulin network in cells, we performed a tubulin degradation assay following **Ru-NAP** treatment using Western blotting. We have tested the expression pattern of the principal cytoskeletal component (tubulin and actin with GAPDH) after **Ru-NAP** treatment, coupled with photoactivation. We detected a significant (4-fold) reduction in the tubulin levels compared to Actin after the cells were treated with **Ru-NAP** (Figure 6c,d). Under similar conditions, both Actin and GAPDH levels remained unchanged (see the quantification). These results provide direct evidence for the tubulin-specific binding and degradation by **Ru-NAP** without perturbation of the actin protein, and the cytotoxicity of the **Ru-NAP** is a result of the combined effect of tubulin/MT disruption and huge site-specific $^1O_2$ generation—a distinct demonstration of CALI.

Cell Cycle Analysis. We examined the cell cycle of MDA-MB-231 cells using PI/RNase staining following incubation with **Rubpy** or **Ru-NAP** (each of 20 μM for 4 h) and photoactivation followed by light irradiation (450 nm, 200 mW·cm^{-2}, 5 min) and incubation for another 48 h. Treatment with **Rubpy + L** or **Ru-NAP + L** induced a noticeable change in the cell cycle profile (Figure 7a). Results for the **Rubpy + L** treatment at 20 μM revealed a G2/M phase arrest (12.2%) compared with the untreated control (11.3%). In contrast, the use of 20 μM **Ru-NAP + L** showed enhanced G2/M phase arrest (24.3%). Docking studies revealed that **Ru-NAP** was bound to the β-tubulin part of the MT more efficiently than

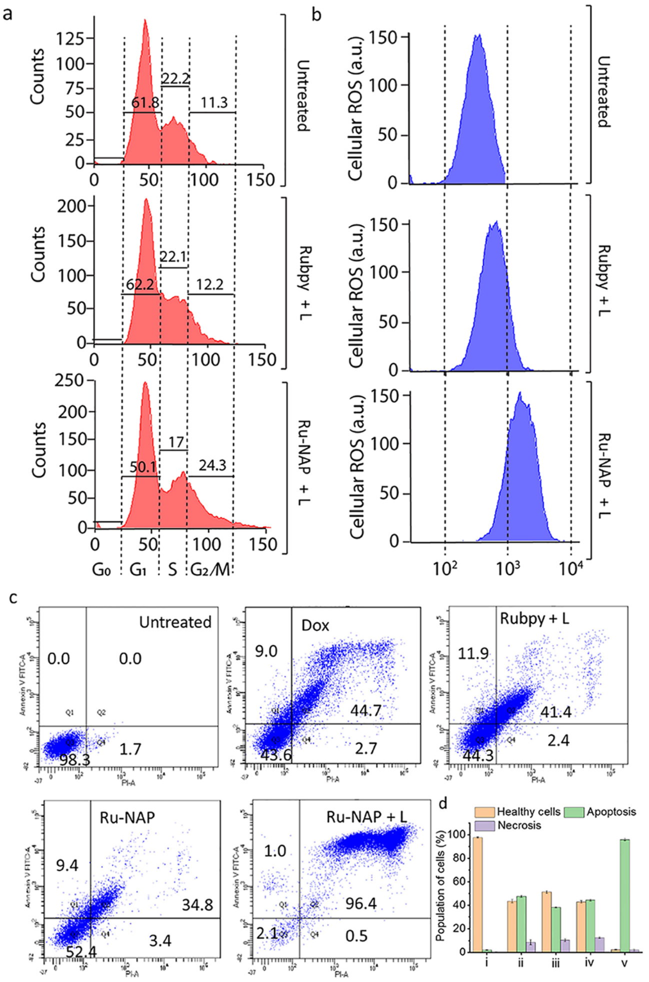

Figure 7. (a) Histograms of the distribution of DNA content by flow cytometric analyses of the **Ru-NAP** mediated cell cycle arrest. (b) Flow cytometry analysis of cellular ROS using CM-H_2DCFDA in MDA-MB231 cells, either untreated or treated with **Rubpy** or **Ru-NAP** (20 μM) separately for 4 h followed by photoactivation (450 nm, 200 mW·cm^{-2}, 5 min, 60 J·cm^{-2}). (c) Analysis of the apoptosis in flow cytometry using dead cell apoptosis kit with Annexin V Alexa Fluor 488 and propidium iodide (PI) (catalogue number: V13241) using Dox (5 μM) as a positive control. **Ru-NAP** induces apoptosis in the MDA-MB-231 cells under dark conditions and after light irradiation (450 nm, 200 mW·cm^{-2}, 5 min, 60 J·cm^{-2}). (d) Histogram of percentages of healthy cells, apoptotic cells, and necrotic cells after different treatments (i: untreated, ii: Dox, iii: **Rubpy + L**, iv: **Ru-NAP**, v: **Ru-NAP + L**) in MDA-MB-231 cells, measured using flow cytometry. The data represent the mean value ± SD obtained from three independent experiments.

NAP and, presumably, this had a pronounced influence in stabilizing tubulin polymerization. This was also consistent with colocalization studies and in vitro tubulin polymerization experiments, which confirmed that **Ru-NAP** could stimulate MT polymerization to disrupt MT dynamics. Seemingly, this interferes with the mitotic spindle assembly during the metaphase/anaphase transition, triggers the mitotic spindle assembly checkpoint, and causes G2/M arrest. Our results are similar to the classical anticancer drugs like Paclitaxel, which induces cell cycle arrest by stabilizing MTs and triggering apoptosis.[95]

Intracellular ROS Generation. Next, we performed flow-cytometry-based analysis to quantify ROS produced in situ due to photoirradiation of live MDA-MB-231 cells after treatment with **Rubpy** or **Ru-NAP** or hydrogen peroxide (H_2O_2) as a positive control using CM-H_2DCFDA. We detected significant ROS production upon exposure to H_2O_2 (500 μM, 12 h; Figure S52). Moreover, a significant increase in intracellular ROS for **Ru-NAP + L** (20 μM) treated cells was observed compared to **Rubpy + L** (Figure 7b). These results are consistent with data showing that **Ru-NAP** is a Type II PDT inducer that generates $^1O_2$ (vide infra) with a relatively high quantum yield of 0.55. These confirmed that the cytotoxicity of **Ru-NAP** was a combination of ROS-induced cell death and significant disruption of MT dynamics. Taken together, **Ru-NAP** destabilized MTs which triggered cell cycle arrest at the G2/M phase along with ROS-induced cell death, which accounted for the observed cellular cytotoxicity ($^{\text{Light}}IC_{50}{}^{\text{Ru-NAP}}$ = 32.5 ± 7.8 nM) in MDA-MB-231 cancer cells.

Flow Cytometry for Analysis of the Apoptosis Pathway. The mode of cell death is an important parameter for any chemotherapeutics drugs. We investigated the cell death pathway induced by **Ru-NAP** by flow cytometry using FITC-Annexin V and Propidium Iodide using Doxorubicin (**Dox**) as a positive control for the induction of apoptosis.[96,97] FITC(−)PI(−) quadrant indicates healthy cells, FITC(+)-PI(−) and FITC(+)PI(+) indicate the apoptotic cells, and FITC(−)PI(+) indicates the necrotic cells. The cells were treated with **Ru-NAP** (1 μM) for 4 h followed by light irradiation (450 nm, 200 mW·cm^{-2}, 5 min, 60 J·cm^{-2}) and kept in the dark for another 20 h. The cells were analyzed in flow cytometry following incubation with annexin V and PI. A significant fraction (97%) of MDA-MB-231 cells underwent the apoptosis process for **Ru-NAP** treated after light irradiation (Figure 7c); 44, 38, and 47% of cells underwent apoptosis after **Rubpy + L**, **Ru-NAP**, and **Dox** treatment, respectively (Figure 7c). Figure 7d shows the histogram of quantitative analysis from the triplicate experiment. This indicated that **Ru-NAP** showed significant apoptosis under dark conditions and almost exclusive light-induced apoptosis of the MDA-MB-231 cells through a combination of disruption of the microtubule/tubulin network dynamics and ROS generation and the efficacy of **Ru-NAP** was more pronounced than **Rubpy**.

In Vivo Studies of Ru-NAP. The PDT efficacy of **Ru-NAP** was further verified in the in vivo MDA-MB-231 xenograft model in nude mice. The MDA-MB-231 cells were inoculated in the right flank of the mice. When the tumor size reached ~100 mm^3, the mice were divided into three groups with n = 5. The groups are (i) untreated, (ii) **Rubpy + L**-treated, and (iii) **Ru-NAP + L**-treated. The mice with an abnormal size were excluded from the study. Then, the mice were treated with **Rubpy** or **Ru-NAP** (2 mg/kg per mouse) intravenously and then kept in the dark for the next 24 h followed by light irradiation for 5 min (450 nm, 200 mW·cm^{-2}, 5 min, 60 J·cm^{-2}). This was repeated every alternative day for 3 weeks. The tumor sizes were measured using a slide caliper, and the tumor volume was calculated using the formula 0.5 x length x width^2 mm^3. The tumor size and the mice's body weight were recorded every third day for 3 weeks. On the 21st day, each mouse was sacrificed, the tumor was isolated and the weight of each tumor was recorded. A significant decrease in the tumor sizes was observed in the **Ru-NAP+ L** treated group compared to the control and **Rubpy + L** (Figure 8a). From the tumor growth ratio curve, 90% and 60% inhibition of the tumor growth was observed in 3 weeks for **Ru-NAP + L**- and **Rubpy + L**-treated groups, respectively, compared to the control (Figure 8b). There was a 90.5 and 56.6% reduction in the tumor weight for the **Ru-NAP + L**- and **Rubpy + L**-treated group, respectively, compared to the control (Figure 8c). We further checked the tumor growth inhibition of **Ru-NAP** (2 mg/kg per mouse) under dark conditions using the MDA-MB-231 xenograft model in nude mice with n = 5 to check the

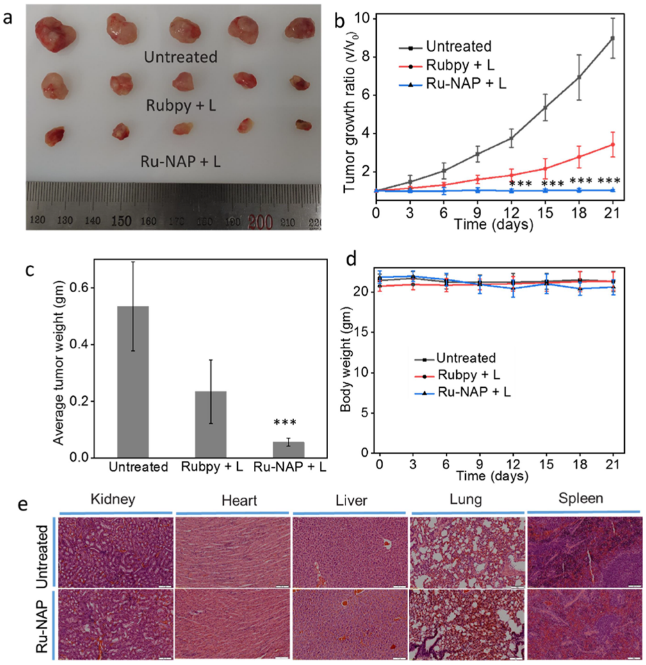

Figure 8. Tumor growth inhibition study of **Ru-NAP** followed by light irradiation (450 nm, 200 mW·cm^{-2}, 5 min, 60 J·cm^{-2}) using MDA-MB-231 tumor xenograft model in balb/c nude mice. (a) The images of the tumor of different group (n = 5) isolated from the mice at 21st day after the treatment. The result showed a significant decrease in the tumor sizes of the **Ru-NAP + L** treated group compared to untreated and **Rubpy + L**. (b) Tumor growth ratio curve of the different treatment group (n = 5). The growth ratio for the **Ru-NAP+ L** treated group is very low compared to those of the untreated and **Rubpy + L**. (c) Histogram of the average tumor weight of the different treatment group (n = 5) as indicated. Tumor weight is too low for **Ru-NAP + L** with respect to that of untreated and **Rubpy + L**. A significant difference was analyzed by comparing with the nonsample-treated control group. * represents $P < 0.05$, ** represents $P < 0.01$, and *** represents $P < 0.001$. The P value was obtained using student's t test. (d) Change in the mice bodyweight of the different treatment group (n = 5) monitored for 3 weeks. (e) H&E staining of the major organs (kidney, heart, liver, lung, and spleen) after **Ru-NAP** treatment in nude mice showing no abnormalities, indicating that **Ru-NAP** is not toxic to the mice.

chemotherapeutic effect of the **Ru-NAP**. The tumor images and tumor growth ratio curve show 50% inhibition of the tumor growth in 3 weeks after Ru-NAP treatment (Figure S53). These data confirmed that **Ru-NAP** could induce tumor growth inhibition under the dark through a chemotherapeutic effect and a more effective growth inhibition through MT disruption, as well as PDT-induced toxicity by $^1O_2$. There was no change in the body weight of the mice after **Ru-NAP** + **L** and **Rubpy** + **L** treatment compared to the control (Figure 8d). Moreover, the H&E staining data of the major organs after **Ru-NAP** treatment do not show any abnormalities (Figure 8e). This indicates that **Ru-NAP** was nontoxic to the mice. The in vivo study further confirmed that **Ru-NAP** possessed a significant tumor inhibition effect with insignificant in vivo toxicity.

CONCLUSIONS

In conclusion, we have demonstrated a proof-of-concept in developing an efficient PDT agent (**Ru-NAP**) for treating TNBC by conjugating a photoactive Ru(II)-polypyridyl moiety, efficient in generating in situ $^1O_2$, to serum stable octapeptide, **NAP**. **NAP** with N-stapled termini and being a short peptide presumably evades proteolytic degradation in blood serum. The TEM images of the **Ru-NAP**/**Py-NAP**/**NAP**, incubated for 5 days, reveal that the fiber formation was most extensive for **Ru-NAP**, which is attributed to a favored cation-π interaction. The metabolic stability of a short peptide, as well as its specificity in binding to the β-tubulin component of a matured microtubule (MT) constitute the rationale for opting for the **NAP** peptide. Specific binding to the β-tubulin of an α, β-tubulin dimer is also examined using docking studies. This confirms stronger interactions between the **Ru-NAP** peptide and β-tubulin compared to **NAP**. Efficient binding with **Ru-NAP** is also established using appropriate binding studies ($K_{\text{Ru-NAP}}$: $(6.8 \pm 0.55) \times 10^6\ \text{M}^{-1}$ and K_{NAP}: $(8.2 \pm 1.1) \times 10^4\ \text{M}^{-1}$). The average linear charge density of ~85 e/nm of MT further favors interaction with the cationic **Rubpy** part of a **Ru-NAP** conjugate accounts for the higher binding constant. Studies with anti-tubulin primary (EP1332Y (1:300; v/v)) and secondary antibody (ab175471, 1:500 (v/v)) with MDA-MB-231 cells, pretreated with **Ru-NAP** and followed by irradiation for 5 min (450 nm, 200 $\text{mW}\cdot\text{cm}^{-2}$, 5 min, 60 $\text{J}\cdot\text{cm}^{-2}$) and then incubation in the dark for 20 h, revealed a noticeable change in the cell cycle profile and cell death. Tubulin polymerization assay (BK006P) confirmed that **Ru-NAP** is effective in stabilizing MT and tubulin polymerization. These account for cell death primarily through cycle arrest in the G2/M phase and cell apoptosis. Apart from the in situ generation of organelle-specific generation of cytotoxic $^1O_2$, fiber formation on the MT surface and/or inside the tubular structure of MT would induce an MT dysfunction and cell death. Control studies reveal that the much lower toxicity of **Ru-NAP** toward HEK293 cells compared to MDA-MB-231 cells (${}^{\text{Light}}\text{IC}_{50}{}^{\text{Ru-NAP}}$[HEK293]: 17.2 ± 2.5 μM, compared to ${}^{\text{Light}}\text{IC}_{50}{}^{\text{Ru-NAP}}$[MDA-MB-231]: 32.5 ± 7.8 nM, ${}^{\text{Dark}}\text{IC}_{50}{}^{\text{Ru-NAP}}$[HEK293]: > 80 μM compared to ${}^{\text{Dark}}\text{IC}_{50}{}^{\text{Ru-NAP}}$[MDA-MB-231]: 2.9 ± 0.5 μM) lies in the accelerated metabolic rate of MDA-MB-231 cells as a result of the Warburg effect coupled with the accumulation of small molecules in cells once they have formed aggregates. Importantly, the Hill plot suggests a cooperative influence of fiber formation on binding to β-tubulin and $^1O_2$ generation in inducing cell death. **Ru-NAP** also shows highly effective tumor growth inhibition in the MDA-MB-231 tumor xenograft model in nude mice. Through this report, we can establish that a new **Ru-NAP** is used effectively for treating TNBC without inducing systemic toxicity.

ASSOCIATED CONTENT

Supporting Information

The Supporting Information is available free of charge at https://pubs.acs.org/doi/10.1021/jacs.4c11820.

> Experimental section; peptide synthesis; Ru-NAP synthesis; characterization; lifetime decay; docking and simulations; tryptophan quenching; DPBF and ABDA assay; lipophilicity; serum stability, morphology in cellular media; cellular uptake and endocytosis; ICP-MS; tubulin colocalization, hill plot, immunocytochemistry, Western blot, cell cycle; DCFDA; annexin V/PI; and in vivo studies (PDF)

AUTHOR INFORMATION

Corresponding Authors

Anitha Ethirajan − *Institute for Materials Research (Imo-imomec), Nanobiophysics and Soft Matter Interfaces (NSI) Group, Hasselt University, B-3500 Hasselt, Belgium; Imec, Imo-imomec, Hasselt University, B-3590 Diepenbeek, Belgium;* orcid.org/0000-0002-2264-2536; Email: anitha.ethirajan@uhasselt.be

Batakrishna Jana − *Department of Chemical Sciences and Center for Advanced Functional Materials, Indian Institute of Science Education and Research (IISER) Kolkata, Mohanpur 741246 West Bengal, India;* Email: bkjdcs88@iiserkol.ac.in

Benu Brata Das − *Laboratory of Molecular Biology, School of Biological Sciences, Indian Association for the Cultivation of Science, Jadavpur, Kolkata 700032 West Bengal, India;* orcid.org/0000-0003-2519-7105; Email: pcbbd@iacs.res.in

Amitava Das − *Department of Chemical Sciences and Center for Advanced Functional Materials, Indian Institute of Science Education and Research (IISER) Kolkata, Mohanpur 741246 West Bengal, India;* orcid.org/0000-0003-3666-1743; Email: amitava@iiserkol.ac.in

Authors

Atin Chatterjee − *Department of Chemical Sciences and Center for Advanced Functional Materials, Indian Institute of Science Education and Research (IISER) Kolkata, Mohanpur 741246 West Bengal, India; Institute for Materials Research (Imo-imomec), Nanobiophysics and Soft Matter Interfaces (NSI) Group, Hasselt University, B-3500 Hasselt, Belgium*

Sandip Sarkar − *Department of Chemical Sciences and Center for Advanced Functional Materials, Indian Institute of Science Education and Research (IISER) Kolkata, Mohanpur 741246 West Bengal, India*

Sangheeta Bhattacharjee − *Laboratory of Molecular Biology, School of Biological Sciences, Indian Association for the Cultivation of Science, Jadavpur, Kolkata 700032 West Bengal, India*

Arpan Bhattacharyya − *Laboratory of Molecular Biology, School of Biological Sciences, Indian Association for the Cultivation of Science, Jadavpur, Kolkata 700032 West Bengal, India*

Surajit Barman − *Department of Chemical Sciences and Center for Advanced Functional Materials, Indian Institute of Science Education and Research (IISER) Kolkata, Mohanpur 741246 West Bengal, India*

Uttam Pal − *Technical Research Centre, S. N. Bose National Centre for Basic Sciences, Salt Lake, Kolkata 700106, India;* orcid.org/0000-0003-2110-4610

Raviranjan Pandey − *Department of Biological Sciences, Indian Institute of Science Education and Research (IISER) Kolkata, Mohanpur 741246 West Bengal, India*

Complete contact information is available at: https://pubs.acs.org/10.1021/jacs.4c11820

Author Contributions

$^\nabla$S.B. and A.B. are contributed equally.

Notes

The authors declare no competing financial interest.

■ ACKNOWLEDGMENTS

A.C. thanks the CSIR for a fellowship and the BOF-BILA program (BOF21BL04) of Hasselt University. A.C. acknowledges IISER Kolkata and Nanobiophysics and Soft Matter Interfaces Laboratory, IMO-IMOMEC, Hasselt University for the infrastructure. A.D. acknowledges the SERB-J.C. Bose Fellowship and funding through the JBR/2023/000005 grant. A.D. also acknowledges the MoE-STARS research grant (No. 2023-47) for financial support. B.J. acknowledges the SERB-Ramanujan Fellowship (RJF/2022/000127) for support. B.B.D. team is supported by the SERB core research grant (CRG/2022/001322), BRNS grant (54/14/10/2022-BRNS/11014), and ICMR grant (2021-11299/CMB/ADHOC-BMS). S.B. acknowledges ICMR-RA Fellowship (45/35/2022-DDI/BMS).

■ REFERENCES

(1) Risinger, A. L.; Giles, F. J.; Mooberry, S. L. Microtubule Dynamics as a Target in Oncology. *Cancer Treat. Rev.* **2009**, *35*, 255−261.

(2) Weaver, B. A. How Taxol/Paclitaxel Kills Cancer Cells. *Mol. Biol. Cell* **2014**, *25*, 2677−2681.

(3) Wang, X.; Gigant, B.; Zheng, X.; Chen, Q. Microtubule-targeting Agents for Cancer Treatment: Seven Binding Sites and Three Strategies. *MedComm Oncol.* **2023**, *2*, No. e46.

(4) Zheng, L.; Ren, R.; Sun, X.; Zou, Y.; Shi, Y.; Di, B.; Niu, M.-M. Discovery of a Dual Tubulin and Poly (ADP-Ribose) Polymerase-1 Inhibitor by Structure-Based Pharmacophore Modeling, Virtual Screening, Molecular Docking, and Biological Evaluation. *J. Med. Chem.* **2021**, *64* (21), 15702−15715.

(5) Shuai, W.; Wang, G.; Zhang, Y.; Bu, F.; Zhang, S.; Miller, D. D.; Li, W.; Ouyang, L.; Wang, Y. Recent Progress on Tubulin Inhibitors with Dual Targeting Capabilities for Cancer Therapy. *J. Med. Chem.* **2021**, *64* (12), 7963−7990.

(6) Dumontet, C.; Jordan, M. A. Microtubule-binding Agents: A Dynamic Field of Cancer Therapeutics. *Nat. Rev. Drug Discovery* **2010**, *9*, 790−803.

(7) Panda, D.; Rathinasamy, K.; Santra, M. K.; Wilson, L. Kinetic Suppression of Microtubule Dynamic Instability by Griseofulvin: Implications for its Possible Use in the Treatment of Cancer. *Proc. Natl. Acad. Sci. U. S. A.* **2005**, *102*, 9878−9883.

(8) Honore, S.; Pasquier, E.; Braguer, D. Understanding Microtubule Dynamics for Improved Cancer Therapy. *Cell. Mol. Life Sci.* **2005**, *62*, 3039−3056.

(9) Gao, L.; Meiring, J. C. M.; Varady, A.; Ruider, I. E.; Heise, C.; Wranik, M.; Velasco, C. D.; Taylor, J. A.; Terni, B.; Weinert, T.; Standfuss, J.; Cabernard, C. C.; Llobet, A.; Steinmetz, M. O.; Bausch, A. R.; Distel, M.; Thorn-Seshold, J.; Akhmanova, A.; Thorn-Seshold, O. In Vivo Photocontrol of Microtubule Dynamics and Integrity, Migration and Mitosis, by The Potent GFP-Imaging-Compatible Photoswitchable Reagents SBTubA4P and SBTub2M. *J. Am. Chem. Soc.* **2022**, *144*, 5614−5628.

(10) Klute, K.; Nackos, E.; Tasaki, S.; Nguyen, D. P.; Bander, N. H.; Tagawa, S. T. Microtubule Inhibitor-based Antibody-drug Conjugates for Cancer Therapy. *Onco Targets Ther.* **2014**, *7*, 2227−2236.

(11) Mukhtar, E.; Adhami, V. M.; Mukhtar, H. Targeting Microtubules by Natural Agents for Cancer Therapy. *Mol. Cancer Ther.* **2014**, *13*, 275−284.

(12) Jordan, M. A.; Wilson, L. Microtubules as a Target for Anticancer Drugs. *Nat. Rev. Cancer.* **2004**, *4*, 253−265.

(13) Pérez-Pérez, M. J.; Priego, E. M.; Bueno, O.; Martins, M. S.; Canela, M. D.; Liekens, S. Blocking Blood Flow to Solid Tumors by Destabilizing Tubulin: an Approach to Targeting Tumor Growth. *J. Med. Chem.* **2016**, *59*, 8685−8711.

(14) Greene, L. M.; Meegan, M. J.; Zisterer, D. M. Combretastatins: More than just Vascular Targeting Agents? *J. Pharmacol. Exp. Ther.* **2015**, *355*, 212−227.

(15) Xiao, H.; Verdier-Pinard, P.; Fernandez-Fuentes, N.; Burd, B.; Angeletti, R.; Fiser, A.; Horwitz, S. B.; Orr, G. A. Insights into the Mechanism of Microtubule Stabilization by Taxol. *Proc. Natl. Acad. Sci. U. S. A.* **2006**, *103*, 10166−10173.

(16) Markman, M. Antineoplastic Agents in the Management of Ovarian Cancer: Current Status and Emerging Therapeutic Strategies. *Trends Pharmacol. Sci.* **2008**, *29*, 515−519.

(17) Sharifi-Rad, J.; Quispe, C.; Patra, J. K.; Singh, Y. D.; Panda, M. K.; Das, G.; Adetunji, C. O.; Michael, O. S.; Sytar, O.; Polito, L.; Živković, J.; Cruz-Martins, N.; Klimek-Szczykutowicz, M.; Ekiert, H.; Choudhary, M. I.; Ayatollahi, S. A.; Tynybekov, B.; Kobarfard, F.; Muntean, A. C.; Grozea, I.; Daştan, S. D.; Butnariu, M.; Szopa, A.; Calina, D. Paclitaxel: Application in Modern Oncology and Nanomedicine-Based Cancer Therapy. *Oxid. Med. Cell. Longev.* **2021**, No. 3687700.

(18) Rohena, C. C.; Mooberry, S. L. Recent Progress with Microtubule Stabilizers: New Compounds, Binding Modes and Cellular Activities. *Nat. Prod. Rep.* **2014**, *31*, 335−355.

(19) Rixel, V. H. S. V.; Ramu, V.; Auyeung, A. B.; Beztsinna, N.; Leger, D. Y.; Lameijer, L. N.; Hilt, S. T.; Dévédec, S. E. L.; Yildiz, T.; Betancourt, T.; Gildner, M. B.; Hudnall, T. W.; Sol, V.; Liagre, B.; Kornienko, A.; Bonnet, S. Photo-Uncaging of a Microtubule-Targeted Rigidin Analogue in Hypoxic Cancer Cells and in a Xenograft Mouse Model. *J. Am. Chem. Soc.* **2019**, *141*, 18444−18454.

(20) Divinski, I.; Holtser-Cochav, M.; Vulih-Schultzman, I.; Steingart, R. A.; Gozes, I. Peptide Neuroprotection through Specific Interaction with Brain Tubulin. *J. Neurochem.* **2006**, *98*, 973−984.

(21) Oz, S.; Kapitansky, O.; Ivashco-Pachima, Y.; Malishkevich, A.; Giladi, E.; Skalka, N.; Rosin-Arbesfeld, R.; Mittelman, L.; Segev, O.; Hirsch, J. A.; Gozes, I. The NAP Motif of Activity-Dependent Neuroprotective Protein (ADNP) Regulates Dendritic Spines through Microtubule End Binding Proteins. *Mol. Psychiatry.* **2014**, *19*, 1115−1124.

(22) Li, Y.; Zhang, H.; Merkher, Y. Recent Advances in Therapeutic Strategies for Triple-Negative Breast Cancer. *J. Hematol. Oncol.* **2022**, *15*, 121.

(23) Bulina, M. E.; Lukyanov, K. A.; Britanova, O. V.; Onichtchouk, D.; Lukyanov, S.; Chudakov, D. M. Chromophore-Assisted Light Inactivation (CALI) using the Phototoxic Fluorescent Protein KillerRed. *Nat. Protoc.* **2006**, *1*, 947−953.

(24) Zhang, L.; Wang, P.; Zhou, X.-Q.; Bretin, L.; Zeng, X.; Husiev, Y.; Polanco, E. A.; Zhao, G.; Wijaya, L. S.; Biver, T.; Le Dévédec, S. E.; Sun, W.; Bonnet, S. Cyclic Ruthenium-Peptide Conjugates as Integrin-Targeting Phototherapeutic Prodrugs for the Treatment of Brain Tumors. *J. Am. Chem. Soc.* **2023**, *145*, 14963−14980.

(25) Cole, H. D.; Vali, A.; Roque, J. A.; Shi, G.; Kaur, G.; Hodges, R. O.; Francés-Monerris, A.; Alberto, M. E.; Cameron, C. G.; McFarland, S. A. Ru (II) Phenanthroline-Based Oligothienyl Complexes as Phototherapy Agents. *Inorg. Chem.* **2024**, *63*, 11450−11458.

(26) Burke, C. S.; Byrne, A.; Keyes, T. E. Targeting Photoinduced DNA Destruction by Ru(II) Tetraazaphenanthrene in Live Cells by Signal Peptide. *J. Am. Chem. Soc.* **2018**, *140*, 6945−6955.

(27) Chakrabortty, S.; Agrawalla, B. K.; Stumper, A.; Vegi, N. M.; Fischer, S.; Reichardt, C.; Kögler, M.; Dietzek, B.; Feuring-Buske, M.; Buske, C.; Rau, S.; Weil, T. Mitochondria Targeted Protein-Ruthenium Photosensitizer for Efficient Photodynamic Applications. *J. Am. Chem. Soc.* **2017**, *139*, 2512−2519.

(28) Jacobson, K.; Rajfur, Z.; Vitriol, E.; Hahn, K. Chromophore-Assisted Laser Inactivation in Cell Biology. *Trends Cell Biol.* **2008**, *18*, 443−450.

(29) Ogorek, A. N.; Zhou, X.; Martell, J. D. Switchable DNA Catalysts for Proximity Labeling at Sites of Protein-Protein Interactions. *J. Am. Chem. Soc.* **2023**, *145*, 16913−16923.

(30) Sato, S.; Morita, K.; Nakamura, H. Regulation of Target Protein Knockdown and Labeling Using Ligand-Directed Ru(bpy)$_3$ Photocatalyst. *Bioconjugate Chem.* **2015**, *26*, 250−256.

(31) Takemoto, K.; Iwanari, H.; Tada, H.; Suyama, K.; Sano, A.; Nagai, T.; Hamakubo, T.; Takahashi, T. Optical Inactivation of Synaptic AMPA Receptors Erases Fear Memory. *Nat. Biotechnol.* **2017**, *35*, 38−47.

(32) Robert, A.; Hill, R. A.; Eyiyemisi, C.; Damisah, E. C.; Chen, F.; Alex, C.; Kwan, A. C.; Grutzendler, J. Targeted Two-Photon Chemical Apoptotic Ablation of Defined Cell Types in Vivo. *Nat. Commun.* **2017**, *8*, No. 15837.

(33) Fu, Z.; Li, S.; Han, S. Antibody Drug Conjugate: the "Biological Missile" for Targeted Cancer Therapy. *Signal Transduction Targeted Ther.* **2022**, *7*, 93.

(34) Beck, A.; Goetsch, L.; Dumontet, C.; Corvaïa, N. Strategies and Challenges for the Next Generation of Antibody-Drug Conjugates. *Nat. Rev. Drug Discovery* **2017**, *16*, 315−337.

(35) Acharya, S.; Maji, M.; Chakraborty, M. P.; Bhattacharya, I.; Das, R.; Gupta, A.; Mukherjee, A. Disruption of the Microtubule Network and Inhibition of VEGFR2 Phosphorylation by Cytotoxic N,O-Coordinated Pt(II) and Ru(II) Complexes of Trimethoxy Aniline-Based Schiff Bases. *Inorg. Chem.* **2021**, *60*, 3418−3430.

(36) Adak, A.; Mohapatra, S.; Mondal, P.; Jana, B.; Ghosh, S. Design of a Novel Microtubule Targeted Peptide Vesicle for Delivering Different Anticancer Drugs. *Chem. Commun.* **2016**, *52*, 7549−7552.

(37) Gong, L.; Zhao, H.; Liu, Y.; Wu, H.; Liu, C.; Chang, S.; Chen, L.; Jin, M.; Wang, Q.; Gao, Z.; Huang, W. Research Advances in Peptide-Drug Conjugates. *Acta Pharm. Sin. B* **2023**, *13*, 3659−3677.

(38) Rizvi, S. F. A.; Zhang, L.; Zhang, H.; Fang, Q. Peptide-Drug Conjugates: Design, Chemistry, and Drug Delivery System as a Novel Cancer Theranostic. *ACS Pharmacol. Transl. Sci.* **2024**, *7*, 309−334.

(39) Plaetzer, K.; Krammer, B.; Berlanda, J.; Berr, F.; Kiesslich, T. Photophysics and photochemistry of photodynamic therapy: fundamental aspects. *Lasers. Med. Sci.* **2009**, *24*, 259−268.

(40) Ghosh, H. N.; Das, A. *Advances in Inorganic Chemistry*; Academic Press-ELSEVIER, 2023; Vol. *81*, pp 305−344.

(41) Yi, X.; Dai, J.; Han, Y.; Xu, M.; Zhang, X.; Zhen, S.; Zhao, Z.; Lou, X.; Xia, F. A high therapeutic efficacy of polymeric prodrug nano-assembly for a combination of photodynamic therapy and chemotherapy. *Commun. Biol.* **2018**, *1*, 202.

(42) Bretin, L.; Husiev, Y.; Ramu, V.; Zhang, L.; Hakkennes, M.; Abyar, S.; Johns, A. C.; Dévédec, S. E. L.; Betancourt, T.; Kornienko, A.; Bonnet, S. Red-Light Activation of a Microtubule Polymerization Inhibitor via Amide Functionalization of the Ruthenium Photocage. *Angew. Chem., Int. Ed.* **2024**, *63*, No. e202316425.

(43) Cao, F.; Wang, H.; Lu, N.; Zhang, P.; Huang, H. A Photoisomerizable Zinc (II) Complex Inhibits Microtubule Polymerization for Photoactive Therapy. *Angew. Chem., Int. Ed.* **2023**, *62*, No. e202301344.

(44) Schmitt, C.; Mauker, P.; Vepřek, N. A.; Gierse, C.; Meiring, J. C. M.; Kuch, J.; Akhmanova, A.; Dehmelt, L.; Thorn-Seshold, O. A Photocaged Microtubule-Stabilising Epothilone Allows Spatiotemporal Control of Cytoskeletal Dynamics. *Angew. Chem., Int. Ed.* **2024**, *63*, No. e202410169.

(45) Sailer, A.; Meiring, J. C. M.; Heise, C.; Pettersson, L. N.; Akhmanova, A.; Thorn-Seshold, J.; Thorn-Seshold, O. Pyrrole Hemithioindigo Antimitotics with Near-Quantitative Bidirectional Photoswitching that Photocontrol Cellular Microtubule Dynamics with Single-Cell Precision. *Angew. Chem., Int. Ed.* **2021**, *60*, 23695.

(46) Elgar, C. E. E.; Yusoh, N. A.; Tiley, P. R.; Kolozsvári, N.; Bennett, L. G.; Gamble, A.; Péan, E. V.; Davies, M. L.; Staples, C. J.; Ahmad, H.; Gill, M. R. Ruthenium (II) Polypyridyl Complexes as FRET Donors: Structure-and Sequence-Selective DNA-Binding and Anticancer Properties. *J. Am. Chem. Soc.* **2023**, *145*, 1236−1246.

(47) B, J.; Zhang, Y.; Wu, S.; Li, H.; Sun, L.; Liu, Y.; Zhu, X.; Qiao, X.; Ma, Q.; Liu, C.; Niu, N.; Xue, J.; Chen, G.; Yang, Y.; Liu, C. KK-LC-1 as a Therapeutic Target to Eliminate ALDH$^+$ Stem Cells in Triple Negative Breast Cancer. *Nat. Commun.* **2023**, *14*, 2602.

(48) Maisch, T.; Baier, J.; Franz, B.; Bäumler, W. The Role of Singlet Oxygen and Oxygen Concentration in Photodynamic Inactivation of Bacteria. *Proc. Natl. Acad. Sci. U. S. A.* **2007**, *104*, 7223−7228.

(49) Carbonaro, M.; Escuin, D.; O'Brate, A.; Thadani-Mulero, M.; Giannakakou, P. Microtubules Regulate Hypoxia-inducible Factor-1α Protein Trafficking and Activity. *J. Biol. Chem.* **2012**, *287*, 11859−11869.

(50) Raza, A.; Archer, S. A.; Fairbanks, S. D.; Smitten, K. L.; Botchway, S. W.; Thomas, J. A.; MacNeil, S.; Haycock, J. W. A Dinuclear Ruthenium (II) Complex Excited by Near-Infrared Light through Two-Photon Absorption Induces Phototoxicity Deep within Hypoxic Regions of Melanoma Cancer Spheroids. *J. Am. Chem. Soc.* **2020**, *142*, 4639−4647.

(51) Heinemann, F.; Karges, J.; Gasser, G. Critical Overview of the Use of Ru(II) Polypyridyl Complexes as Photosensitizers in One-Photon and Two-Photon Photodynamic Therapy. *Acc. Chem. Res.* **2017**, *50*, 2727−2736.

(52) Li, X.; Kwon, N.; Guo, T.; Liu, Z.; Yoon, J. Innovative Strategies for Hypoxic-Tumor Photodynamic Therapy. *Angew. Chem., Int. Ed.* **2018**, *57*, 11522−11531.

(53) Ghosh, A.; Das, P.; Gill, M. R.; Kar, P.; Walker, M. G.; Thomas, J. A.; Das, A. Photoactive Ru^{II}-Polypyridyl Complexes that Display Sequence Selectivity and High-Affinity Binding to Duplex DNA through Groove Binding. *Chem.—Eur. J.* **2011**, *17*, 2089−2098.

(54) Poynton, F. E.; Bright, S. A.; Blasco, S.; Williams, D. C.; Kelly, J. M.; Gunnlaugsson, T. The Development of Ruthenium (II) Polypyridyl Complexes and Conjugates for in Vitro Cellular and in Vivo Applications. *Chem. Soc. Rev.* **2017**, *46*, 7706−7756.

(55) Bonnet, S. Ruthenium-Based Photoactivated Chemotherapy. *J. Am. Chem. Soc.* **2023**, *145*, 23397−23415.

(56) Goodson, H. V.; Jonasson, E. M. Microtubules and Microtubule-Associated Proteins. *Cold Spring Harb. Perspect. Biol.* **2018**, *10*, a022608.

(57) Sekulić, D. L.; Satarić, M. V. An Improved Nanoscale Transmission Line Model of Microtubule: The Effect of Nonlinearity on the Propagation of Electrical Signals. *Elec. Energy* **2015**, *28*, 133−142.

(58) Minoura, I.; Muto, E. Dielectric Measurement of Individual Microtubules Using the Electroorientation Method. *Biophys. J.* **2006**, *90*, 3739−3748.

(59) Adak, A.; Das, G.; Barman, S.; Mohapatra, S.; Bhunia, D.; Jana, B.; Ghosh, S. Biodegradable Neuro-Compatible Peptide Hydrogel Promotes Neurite Outgrowth, Shows Significant Neuroprotection, and Delivers Anti-Alzheimer Drug. *ACS Appl. Mater. Interfaces.* **2017**, *9*, 5067−5076.

(60) Pierce, S.; Jennings, M. P.; Juliano, S. A.; Angeles-Boza, A. M. Peptide-Ruthenium Conjugate as an Efficient Photosensitizer for the Inactivation of Multidrug-Resistant Bacteria. *Inorg. Chem.* **2020**, *59*, 14866−14870.

(61) Kandoth, N.; Chaudhary, S.; Gupta, S.; Raksha, K.; Chatterjee, A.; Gupta, S.; Karuthedath, S.; Castro, C. D.; Laquai, F.; Pramanik, S. K.; Bhattacharyya, S.; Mallick, A. I.; Das, A. Multimodal Biofilm Inactivation Using a Photocatalytic Bismuth Perovskite-TiO$_2$-Ru(II)-polypyridyl-Based Multisite Heterojunction. *ACS Nano* **2023**, *17*, 10393−10406.

(62) Banerjee, T.; Rawalekar, S.; Das, A.; Ghosh, H. N. Interfacial Electron Transfer Dynamics of Two Newly Synthesized Catecholate Bound Ru^{II} Polypyridyl-Based Sensitizers on TiO_2 Nanoparticle Surface-A Femtosecond Pump Probe Spectroscopic Study. *Eur. J. Inorg. Chem.* **2011**, *2011*, 4187−4197.

(63) Mahato, P.; Saha, S.; Choudhury, S.; Das, A. Solvent-Dependent Aggregation Behavior of a New Ru (II)-Polypyridyl Based Metallo surfactant. *Chem. Commun.* **2011**, *47*, 11074−11076.

(64) Zhang, K. Y.; Yu, Q.; Wei, H.; Liu, S.; Zhao, Q.; Huang, W. Long-Lived Emissive Probes for Time-Resolved Photoluminescence Bioimaging and Biosensing *Chem. Rev.* **2018**, *118*, 1770−1839.

(65) Shum, J.; Leung, P. K-K.; Lo, K. K-W. Luminescent Ruthenium (II) Polypyridine Complexes for a Wide Variety of Biomolecular and Cellular Applications. *Inorg. Chem.* **2019**, *58*, 2231−2247.

(66) Byrne, A.; Burkeab, C. S.; Keyes, T. E. Precision Targeted Ruthenium (II) Luminophores; Highly Effective Probes for Cell Imaging by Stimulated Emission Depletion (STED) Microscopy. *Chem. Sci.* **2016**, *7*, 6551−6562.

(67) Martin, A.; Byrne, A.; Burke, C. S.; Forster, R. J.; Keyes, T. E. Peptide-Bridged Dinuclear Ru (II) Complex for Mitochondrial Targeted Monitoring of Dynamic Changes to Oxygen Concentration and ROS Generation in Live Mammalian Cells. *J. Am. Chem. Soc.* **2014**, *136*, 15300−15309.

(68) Gozes, I.; Morimoto, B. H.; Tiong, J.; Fox, A.; Sutherland, K.; Dangoor, D.; Holser-Cochav, M.; Vered, K.; Newton, P.; Aisen, P. S.; Matsuoka, Y.; Dyck, C. H. V.; Thal, L. NAP: Research and Development of a Peptide Derived from Activity-Dependent Neuroprotective Protein (ADNP). *CNS Drug Rev.* **2005**, *11*, 353−368.

(69) Yammine, A.; Gao, J.; Kwan, A. H. Tryptophan Fluorescence Quenching Assays for Measuring Protein-ligand Binding Affinities: Principles and a Practical Guide. *Bio Protoc.* **2019**, *9*, No. e3253.

(70) Chakraborti, S.; Das, L.; Kapoor, A. N.; Dwivedi, V.; Poddar, A.; Chakraborti, G.; Janik, M.; Basu, G.; Panda, D.; Chakrabarti, P.; Surolia, A.; Bhattacharyya, B. Curcumin Recognizes a Unique Binding Site of Tubulin. *J. Med. Chem.* **2011**, *54*, 6183−6196.

(71) Jana, B.; Mohapatra, S.; Mondal, P.; Barman, S.; Pradhan, K.; Saha, A.; Ghosh, A. α-Cyclodextrin Interacts Close to Vinblastine Site of Tubulin and Delivers Curcumin Preferentially to the Tubulin Surface of Cancer Cell. *ACS Appl. Mater. Interfaces.* **2016**, *8*, 13793−13803.

(72) Gupta, K.; Panda, D. Perturbation of Microtubule Polymerization by Quercetin through Tubulin Binding: A Novel Mechanism of its Antiproliferative Activity. *Biochemistry.* **2002**, *41*, 13029−13038.

(73) Biswas, A.; Kurkute, P.; Jana, B.; Laskar, A.; Ghosh, S. An Amyloid Inhibitor Octapeptide forms Amyloid Type Fibrous Aggregates and Affects Microtubule Motility. *Chem. Commun.* **2014**, *50*, 2604−2607.

(74) Ashur-Fabian, O.; Segal-Ruder, Y.; Skutelsky, E.; Brenneman, D. E.; Steingart, R. A.; Giladi, E.; Gozes, I. The Neuroprotective Peptide NAP Inhibits the Aggregation of the Beta-Amyloid Peptide. *Peptides* **2003**, *24*, 1413−1423.

(75) Przybyla, D. E.; Chmielewski, J. Metal-Triggered Radial Self-Assembly of Collagen Peptide fibers. *J. Am. Chem. Soc.* **2008**, *130*, 12610−12611.

(76) Entradas, T.; Waldrona, S.; Volk, M. The Detection Sensitivity of Commonly Used Singlet Oxygen Probes in Aqueous Environments. *J. Photochem. Photobiol., B* **2020**, *204*, No. 111787.

(77) Lindig, B. A.; Rodgers, M. A. J.; Paul Schaap, A. Determination of the Lifetime of Singlet Oxygen in D_2O Using 9,10-Anthracenedipropionic Acid, a Water-Soluble Probe. *J. Am. Chem. Soc.* **1980**, *102*, 5590−5593.

(78) Ramu, V.; Aute, S.; Taye, N.; Guha, R.; Walker, M. G.; Mogare, D.; Parulekar, A.; Thomas, J. A.; Chattopadhyay, S.; Das, A. Photo-Induced Cytotoxicity and Anti-Metastatic Activity of Ruthenium(II)-Polypyridyl Complexes Functionalized with Tyrosine or Tryptophan. *Dalton Trans.* **2017**, *46*, 6634−6644.

(79) Han, G.; Li, G.; Huang, J.; Han, C.; Turro, C.; Sun, Y. Two-Photon-Absorbing Ruthenium Complexes Enable Near Infrared Light-Driven Photocatalysis. *Nat. Commun.* **2022**, *13*, 2288.

(80) Toupin, N.; Steinke, S. J.; Nadella, S.; Li, A.; Rohrabaugh, T. N.; Samuels, E. R.; Turro, C.; Sevrioukova, I. F.; Kodanko, J. J. Photosensitive Ru(II) Complexes as Inhibitors of the Major Human Drug Metabolizing Enzyme CYP3A4. *J. Am. Chem. Soc.* **2021**, *143*, 9191−9205.

(81) Acharya, S.; Maji, M.; Chakraborty, M. P.; Bhattacharya, I.; Das, R.; Gupta, A.; Mukherjee, A. Disruption of Microtubule Network and Inhibition of VEGFR2 Phosphorylation by Cytotoxic N,O Coordinated Pt(II) and Ru(II) Complexes of Trimethoxy Aniline Based Schiff Bases. *Inorg. Chem.* **2021**, *60*, 3418−3430.

(82) van Rijt, S. H.; Mukherjee, A.; Pizarro, A. M.; Sadler, P. J. Cytotoxicity, Hydrophobicity, Uptake, and Distribution of Osmium-(II) Anticancer Complexes in Ovarian Cancer Cells. *J. Med. Chem.* **2010**, *53*, 840−849.

(83) Zhang, R.; Qin, X.; Kong, F.; Chen, P.; Pan, G. Improving Cellular Uptake of Therapeutic Entities through Interaction with Components of Cell Membrane. *Drug Delivery* **2019**, *26*, 328−342.

(84) Mitchell, M. J.; Billingsley, M. M.; Haley; Wechsler, M. E.; Peppas, N. A.; Langer, R. Engineering Precision Nanoparticles for Drug Delivery. *Nat. Rev. Drug Discovery* **2021**, *20*, 101−124.

(85) Bhargava, S.; Kulkarni, R.; Dewangan, B.; Jiaswar, C.; Kumar, K.; Kumar, A.; Kulkarni, N.; Bodhe, P. R.; Kumarb, H.; Sahu, B. Microtubule Stabilising Peptides: New Paradigm towards Management of Neuronal Disorders. *RSC Med. Chem.* **2023**, *14*, 2192−2205.

(86) Silva, S.; Almeida, A. J.; Vale, N. Combination of Cell-Penetrating Peptides with Nanoparticles for Therapeutic Application: A Review. *Biomol.* **2019**, *9*, 22.

(87) Liu, K.; Newbury, P. A.; Glicksberg, B. S.; Zeng, W. Z. D.; Paithankar, S.; Andrechek, E. R.; Chen, B. Evaluating Cell Lines as Models for Metastatic Breast Cancer through Integrative Analysis of Genomic Data. *Nat. Commun.* **2019**, *10*, 2138.

(88) Gao, Y.; Shi, J.; Yuan, D.; Xu, B. Imaging Enzyme-Triggered Self-Assembly of Small Molecules inside Live Cells. *Nat. Commun.* **2012**, *3*, 1033.

(89) Bigman, L. S.; Levy, Y. Protein Diffusion on Charged Biopolymers: DNA Versus Microtubule. *Biophys. J.* **2020**, *118*, 3008−3018.

(90) Hsu, P. P.; Sabatini, D. M. Cancer Cell Metabolism: Warburg and Beyond. *Cell.* **2008**, *134*, 703−707.

(91) Yang, Z. M.; Liang, G. L.; Guo, Z. F.; Guo, Z. H.; Xu, B. Intracellular Hydrogelation of Small Molecules Inhibits Bacterial Growth. *Angew. Chem., Int. Ed.* **2007**, *46*, 8216−8219.

(92) Kuang, Y.; Xu, B. Disruption of the Dynamics of Microtubules and Selective Inhibition of Glioblastoma Cells by Nanofibers of Small Hydrophobic Molecules. *Angew. Chem., Int. Ed.* **2013**, *52*, 6944−6948.

(93) D'Amato, A.; Mariconda, A.; Iacopetta, D.; Ceramella, J.; Catalano, A.; Sinicropi, M. S.; Longo, P. Complexes of Ruthenium(II) as Promising Dual-Active Agents against Cancer and Viral Infections. *Pharmaceuticals.* **2023**, *16*, 1729.

(94) Verlato, G.; Cerveri, I.; Villani, A.; Pasquetto, M.; Ferrari, M.; Fanfulla, F.; Zanolin, E.; Rijcken, B.; Marco, R. Evaluation of Methacholine Dose-Response Curves by Linear and Exponential Mathematical Models: Goodness-of-Fit and Validity of Extrapolation. *Eur. Respir. J.* **1996**, *9*, 506−511.

(95) Wang, C.; Huang, S.-B.; Yang, M.-C.; Lin, Y.-T.; Chu, I.-H.; Shen, Y.-N.; Chiu, Y.-H.; Hung, S.-H.; Kang, L.; Hong, Y.-R. Combining Paclitaxel with ABT-263 Has a Synergistic Effect on Paclitaxel Resistant Prostate Cancer Cells. *PLoS One.* **2015**, *10*, No. e0120913.

(96) De, K. Decapeptide Modified Doxorubicin Loaded Solid Lipid Nanoparticles as Targeted Drug Delivery System against Prostate Cancer. *Langmuir.* **2021**, *37*, 13194−13207.

(97) Sarkar, S.; Chatterjee, A.; Kim, D.; Saritha, C.; Barman, S.; Jana, B.; Ryu, J.-H.; Das, A. Host-Guest Adduct as a Stimuli-responsive Prodrug: Enzyme-Triggered Self-Assembly Process of a Short Peptide

within Mitochondria to Induce Cell Apoptosis. *Adv. Healthcare Mater.* **2024**, No. 2403243.